

PRESERVATION OF ORIGINAL SEDIMENTARY SULFUR
ISOTOPE RECORDS UNDER POST-DEPOSITIONAL
THERMAL ALTERATION

by

Hanna Konavaluk

A thesis submitted in partial fulfillment of

the requirements for the degree of

Master of Science

(Geoscience)

at the

UNIVERSITY OF WISCONSIN-MADISON

2025

Acknowledgements

This work would not have been possible without the continued support of my committee, colleagues, friends, and family.

I want to first acknowledge the unconditional support of my advisor Selva Marroquín, without whom this work would not exist. Thank you for trusting me with this project and always having faith in me. I am so grateful for the support of my committee members Steve Meyers and Chloe Bonamici. Thank you to Steve Meyers, for fostering my scientific curiosity as well as my love of teaching, and to Chloe Bonamici, for lending her expertise in metamorphic petrology and SIMS analysis. I want to acknowledge the help of Tyler Blum, Bryan Wathan, and Bil Schnieder. Without their expertise, none of the analyses for this project would have been completed. To my wonderful lab mates Kayla McCabe and Maya Roselli, thank you for always cheering me on and providing excellent feedback.

None of this work would have been possible without the support of my friends, both in and outside of the Geoscience Department. In particular, I would like to thank my friends and officemates Sophia Pinter, for a constant supply of laughter and coffee breaks; Aidan Lewandowski, who simply gives the best advice; and Abby Santis, who never fails to make me laugh. A special thank you to my lifelong friend Molly Lecher, who has truly been here through it all.

I am so grateful for the unconditional support of Maggie Cremers. I can't thank you enough for always being there for me and for making Madison feel like home. I want to acknowledge the support of Sue Franzen, whom I will always look up to. Thank you for being a grounding presence in my life and for giving me a peaceful place to write this thesis. Lastly, thank you to my parents, Mary and Steve, who don't believe in deep time, but have always believed in me.

Table of Contents

Abstract	v
Introduction	vi
I. Significance.....	vi
II. Global sulfur cycle & paleoenvironment reconstruction.....	1
III. Pyrite formation.....	2
IV. Sulfur isotope fractionation.....	3
V. Inherent pyrite $\delta^{34}\text{S}$ variability.....	9
VI. Post-depositional alteration of sulfur records.....	9
VII. Study overview.....	12
VIII. Geologic Setting.....	13
Materials and methods	15
I. Sample collection and preparation.....	15
II. Acid insoluble carbon and sulfur content.....	17
III. Bulk sulfur and carbon content.....	18
IV. Mineralogy.....	18
V. Sulfide grain characterization.....	18
VI. In situ sulfur isotope analysis.....	21
Results	22
I. Thermal maturity constraints.....	22
A. Carbon content and acid soluble content.....	22
B. Sulfur content.....	23
C. Mineralogy.....	24
II. Sulfide grain characterization.....	26
III. In situ sulfur isotope analysis.....	34
A. Inter-grain $\delta^{34}\text{S}$ variability.....	34

B. Intra-grain $\delta^{34}\text{S}$ variability.....	38
Discussion.....	38
I. Characterization of the Pierre Shale.....	38
A. Post-depositional thermal alteration.....	39
i. Total organic carbon geothermometry.....	40
ii. Clay mineral geothermometry.....	41
B. Sulfide grain characterization.....	43
II. In situ sulfur isotope analysis.....	45
A. Sulfide $\delta^{34}\text{S}$	45
B. Pyrite and pyrrhotite $\delta^{34}\text{S}$	47
III. Effects of thermal alteration on sedimentary sulfur records.....	49
A. Heterogeneity of metamorphic fluid flow.....	49
B. Sulfur exchange with metamorphic fluids.....	55
Conclusions.....	58
References.....	61

Note on sample repository items:

All specimens referred to in this dissertation are in the collections of the Department of Geoscience, University of Wisconsin-Madison, under file number **UW2057**.

Abstract

The sedimentary sulfur record is critical for interpreting how marine environments have evolved throughout Earth's history because the burial of reduced sulfur species (i.e. in pyrite and kerogen) impacts global climate through drawdown of atmospheric CO₂ and buildup of O₂ levels. Furthermore, depositional conditions, such as ocean chemistry, microbial activity, and redox conditions in deep geologic time are recorded in the pyrite sulfur isotope composition (i.e. $\delta^{34}\text{S}$). Microbial sulfate reduction, a key step in pyrite formation, imparts an isotopic fractionation that is preserved in pyrite $\delta^{34}\text{S}$. This process occurs in low-oxygen environments when other metabolic processes, such as aerobic respiration, are unavailable to organisms. Thus, the deposition of sulfur as pyrite in the sedimentary record can indicate periods of anoxia in marine environments through time. However, it remains unclear whether original $\delta^{34}\text{S}$ signals are retained after deep burial and exposure to the geothermal gradient, and later stage metamorphism. This is important to distinguish as use of the sedimentary sulfur record is limited by the uncertainty in how these records are impacted by post-depositional alteration. In this work I seek to assess how well sedimentary $\delta^{34}\text{S}$ records are preserved under high temperature diagenesis through metamorphic conditions, using in-situ sulfur isotope analyses of $\delta^{34}\text{S}$ of individual pyrite grains.

Samples were collected within a single stratigraphic horizon of the Upper Cretaceous Pierre Shale (Raton Basin, NM) along a transect perpendicular to a later igneous intrusion, in which heating decreased with distance from the dike. I collected Secondary Ionization Mass Spectrometry (SIMS) data on individual pyrite grains and additional mineralogical and lithological constraints (e.g. x-ray diffraction, total organic carbon content, and total sulfur content). I find that sedimentary sulfur isotope signatures in the Pierre Shale remain preserved

across metamorphic grades up to $\sim 300^{\circ}\text{C}$. Heterogeneous fluid flow produced an irregular spatial distribution of sulfide minerals across the outcrop as pyrite reacted to form pyrrhotite, and increasing bulk sulfur contents toward the dike suggests magmatic sulfur addition.

Although heating recrystallized pyrite from framboids to larger crystals, sulfur-rich magmatic fluids may have limited sulfur exchange, potentially contributing to the preservation of original $\delta^{34}\text{S}$ signature across the gradient. This work supports interpretations of measured $\delta^{34}\text{S}$ values of sediments in contact metamorphic setting, increasing confidence in $\delta^{34}\text{S}$ measurements on rocks previously deemed unsuitable for analysis and interpretation.

Introduction

I. Significance

Sulfur is a critical element in global marine biogeochemical cycles and is primarily present as sulfate (SO_4^{2-}), the second most abundant anion in seawater. Throughout Earth's history, sulfur has played a dynamic role—from shaping the early evolution of Earth's biosphere to shaping our modern biogeochemical cycles (Fakraee et al., 2024). The preservation of reduced sulfur as pyrite in sediments has direct implications for global climate due to the interwoven nature of the sulfur, carbon, and oxygen cycles; these relationships have been leveraged to reconstruct paleoenvironment through time (Berner and Canfield, 1989). Further, there is information on marine redox conditions, marine chemistry, nutrient cycling, and primarily productivity changes throughout Earth's history contained in the pyrite grains themselves—within its stable sulfur isotope composition (i.e. $\delta^{34}\text{S}$) (Berner, 1984; Fakraee et al., 2024). However, as these sediments undergo thermal alteration, it is unclear how the pyrite $\delta^{34}\text{S}$ is affected. Studying the preserved sulfur isotope composition of Fe-sulfides, and assessing its sensitivity to thermal overprinting, allows us to separate original depositional signals from post-depositional alteration.

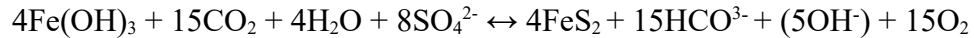
This distinction strengthens our interpretive understanding of how sulfur cycling in past marine systems responds to natural perturbations and helps inform predictions of how modern biogeochemical cycles will react under continued environmental change.

II. Global sulfur cycle & paleoenvironment reconstruction

To understand the biogeochemical cycling of sulfur in the oceans, we first can evaluate the inputs and outputs of sulfur to the marine system. Inputs of sulfur to the marine environment include continental weathering of sulfides in the continental crust, volcanism, and hydrothermal vents; outputs include the incorporation and burial of sulfate in carbonates, evaporites, and burial of reduced sulfur species. These inputs and outputs have not been balanced 1:1 with time; rather, the concentration of marine sulfate has been significantly lower than modern marine sulfate values, which today average 28 mM, for much of Earth's history (Fakraee et al., 2024). Marine sulfate concentrations remained low but variable, ranging between 10-10³ μM, before climbing to modern-like high sulfate levels in the Phanerozoic due to changes in Earth's redox state (Fakraee et al., 2024). Changes in seawater sulfate levels are directly related to the relative fluxes in and out of the marine system. This study focuses one of those major fluxes out of the marine system—specifically, the removal of sulfur via the burial of reduced sulfur compounds such as pyrite.

Pyrite burial represents a key intersection of the sulfur, carbon, and oxygen cycles (Berner, 1982; Werne et al., 2004; Fakraee et al., 2024). It results in the net removal of CO₂ and release of O₂, significantly affecting the interconnected biogeochemical cycles of sulfur, carbon, and oxygen—and thus impacting the global climate (Eqn. 1) (Berner, 1982; Werne et al., 2004; Fakraee et al., 2024). Pyrite burial only occurs under reducing conditions; therefore researchers have worked to

understand when this output flux operates and how it changes in Earth's history to reconstruct paleoenvironmental conditions through time, (e.g. expanded marine anoxia conditions).



Equation 1. Drawdown of CO_2 and buildup of O_2 through pyrite burial (Werne et al., 2004).

III. Pyrite Formation

Sulfur enters marine environments primarily as sulfate (SO_4^{2-}) but must be reduced before it can be buried as pyrite (Fakhraee et al., 2024). The formation of sedimentary pyrite occurs during early diagenesis (Berner, 1984) at, or below, the sediment-water interface, where microbes use sulfate reduction as an energy source when other respiration processes—such as oxygen, nitrate, manganese, or iron reduction—are unavailable or unfavorable (Owens, 2019). This indicates that sulfate reduction occurs in anoxic environments with limited concentrations of nitrate, manganese, or iron (FeOOH).

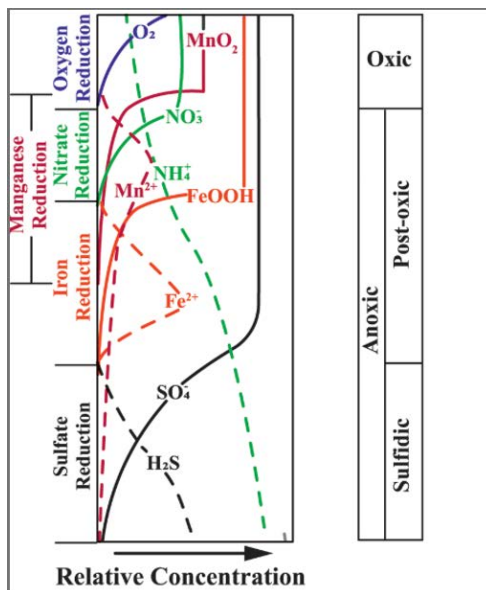
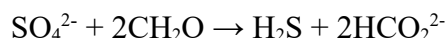


Figure 1. Redox ladder showing oxygen, nitrate, manganese, iron, and sulfate reduction (Owens, 2019).

During this process of microbial sulfate reduction (MSR), sulfate reacts with organic matter (CH₂O) to form reduced hydrogen sulfide (H₂S) and carbon dioxide (CO₂) (Werne et al., 2004). MSR is a redox reaction in which microbes gain energy through the exchange of electrons during the reduction of sulfate and oxidation of organic material (Fig. 1). When exposed to highly reactive iron species, especially Fe hydroxides, hydrogen sulfide will readily react to form pyrite (Canfield, 2001). Limiting factors for the production and burial of pyrite include the supply of reactive organic matter, concentration of dissolved sulfate, and abundance of reactive iron minerals (Berner, 1984).



Equation 2. Sulfate reduction reactions (Canfield, 2001).

Though not the focus of this study, it is important to note that in the absence, or limitation, of reactive iron species, hydrogen sulfide or reactive intermediate sulfur species (e.g. S_xO_y, S⁰, HS_x⁻) can instead be incorporated into organic matter during diagenesis to form sulfurized organic matter that can be preserved as an additional sink of reduced sulfur and another δ³⁴S record (Werne et al., 2003; Raven et al., 2023).

IV. Sulfur isotope fractionation

Sulfur has four stable isotopes—³²S, ³³S, ³⁴S, and ³⁶S—with respective abundances of ~95.02%, ~0.75%, ~4.21%, and ~0.02% (Wieser and Brand, 1999). Sulfur is globally ubiquitous, with

major reservoirs in the core, mantle, oceans, and the crustal rock record. The S isotope composition of marine sediments can reflect depositional environmental conditions and is widely used in paleoenvironmental reconstruction. Evaporites and carbonates generally archive the sulfur isotope composition of seawater, whereas clastic marine sediments (referred to as “sediments” here) record isotopic fractionation that reflects marine redox conditions. In particular, variations in ^{32}S and ^{34}S provide key insights for paleoenvironmental interpretation and are the focus of this section.

The isotope composition of seawater sulfate is known to have changed over time (Fakhraee et al., 2024). More specifically, the relative concentration of ^{34}S to ^{32}S , denoted as $\delta^{34}\text{S}$ (Eqn. 3), has changed. This is the result of either a change in the magnitude of the fluxes of sulfur into and out of the oceans or due to a change in the isotope fractionation between sulfate and buried sulfide (Fig. 2) (Bottrell and Newton, 2006).

$$\delta^{34}\text{S} = \left(\frac{{}^{34}\text{S}/{}^{32}\text{S}}{\text{sample}} / \frac{{}^{34}\text{S}/{}^{32}\text{S}}{\text{standard}} \right) \times 1000$$

Equation 3. Calculation of $\delta^{34}\text{S}$ (Thode et al., 1961).

The sulfate-sulfide fractionation (3‰ to 46‰) is imparted by microbes that facilitate MSR—the results of which are preserved in the sulfur isotope composition of pyrite grains (Jones and Starkey, 1957; Harrison and Thode, 1958; Kaplan and Rittenberg, 1964; Canfield and Teske, 1996; Canfield, 2001). MSR results in hydrogen sulfide that is depleted in ^{34}S relative to the source sulfate. This means that the resulting pyrite will have a lower $\delta^{34}\text{S}$ value relative to the starting isotopic composition of sulfate.

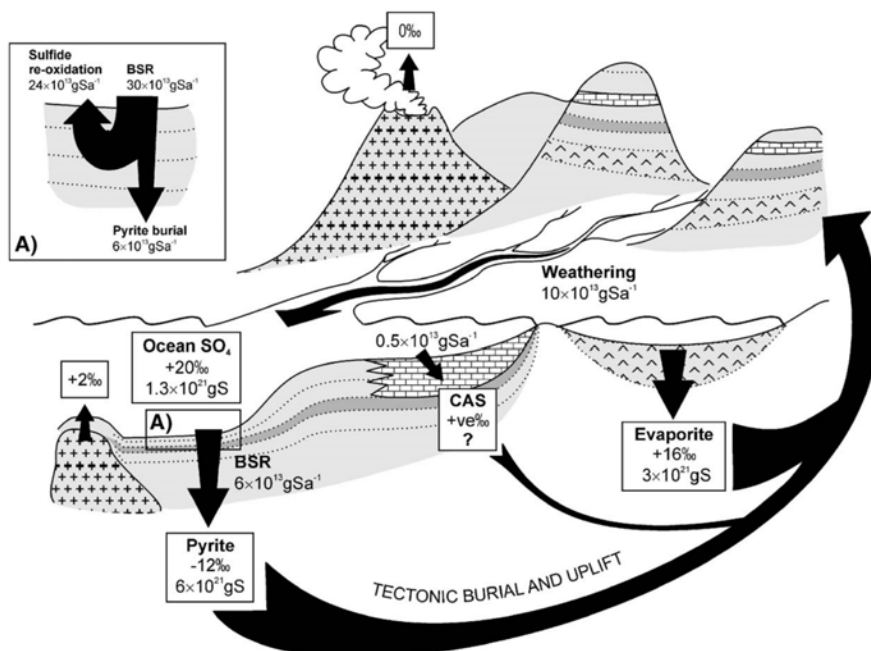


Figure 2. A schematic of the sulfur cycle and sulfur reservoirs isotope composition where BSR = bacterial sulfate reduction and CAS = carbonate-associated sulfur (Bottrell and Newton, 2006).

The sedimentary sulfur record, preserved in pyrite $\delta^{34}\text{S}$, is a record of local depositional conditions, which have been leveraged to interpret paleoenvironment in deep time (Berner, 1978; Maynard, 1980; Canfield, 2004). Factors that can influence the extent of sulfur isotope fractionation that is recorded in pyrite $\delta^{34}\text{S}$, include (1) marine redox conditions, (2) sedimentation rate, (3) rate of sulfate reduction, and (4) electron donor species, (5) depth of formation, and (6) sulfate availability (Maynard, 1980; Berner, 1984; Werne et al., 2003; Fike et al., 2015a). (1) Regarding marine redox conditions, the extent of sulfur isotope fractionation produced by MSR indicates that the sediments experienced anoxic conditions (Canfield, 2001b; Werne et al., 2003). (2) Sedimentation rate is thought to have an inverse relationship with sulfur fractionation, with increasing fractionation associated with lower rates of sedimentation

(Maynard, 1980; Gautier, 1985). This relationship is due to the rate of MSR increasing with increasing sedimentation rates, as well as the fact that microbes impart less isotopic fractionation at higher rates of MSR, resulting in H₂S that is more enriched in ³⁴S relative to H₂S produced at lower rates of MSR (Maynard, 1980). It should also be noted that the cell-specific rate of sulfate reduction (mol cell⁻¹ time⁻¹) is temperature dependent, increasing as temperatures rise (Canfield, 2001b). Electron donor species can play a role in fractionations, where higher fractionations can result from H₂ as an electron donor as opposed to organic matter (Eqn. 2) (Berner, 1984). In a closed system environment of sulfate reduction, a Rayleigh-type distillation occurs, which results in parallel shifts in pyrite and sulfate δ³⁴S reflecting the fractionation from MSR (epsilon: ~25 per mil average) (Fike et al., 2015). As sulfate reduction proceeds deeper in the sediment column, the residual sulfate pool concentration decreases and the sulfate δ³⁴S increases; simultaneously, the pyrite pool increases and the average pyrite δ³⁴S also increases (Fig. 3) (Fike et al., 2015). Assuming no exchange between the pore water sulfate pool and the overlying water column, this distillation produces a constant instantaneous fractionation between the sulfate and sulfide, with average bulk pyrite δ³⁴S values approaching initial sulfate δ³⁴S values (Fig. 3) (Fike et al., 2015a). This Rayleigh-type distillation proceeding in the sediment column influences the pyrite δ³⁴S preserved in marine sediments. Lastly, higher fractionations, up to 46‰ (average ~18‰), have been reported as a result of abundant sulfate (>1mM) concentrations (Canfield and Teske, 1996). In addition, species- and enzyme-specific pathways of sulfate reduction and disproportionation (discussed below) can strongly influence the magnitude of sulfur isotope fractionation that is preserved in sediments (Canfield, 2001; Leavitt, 2014).

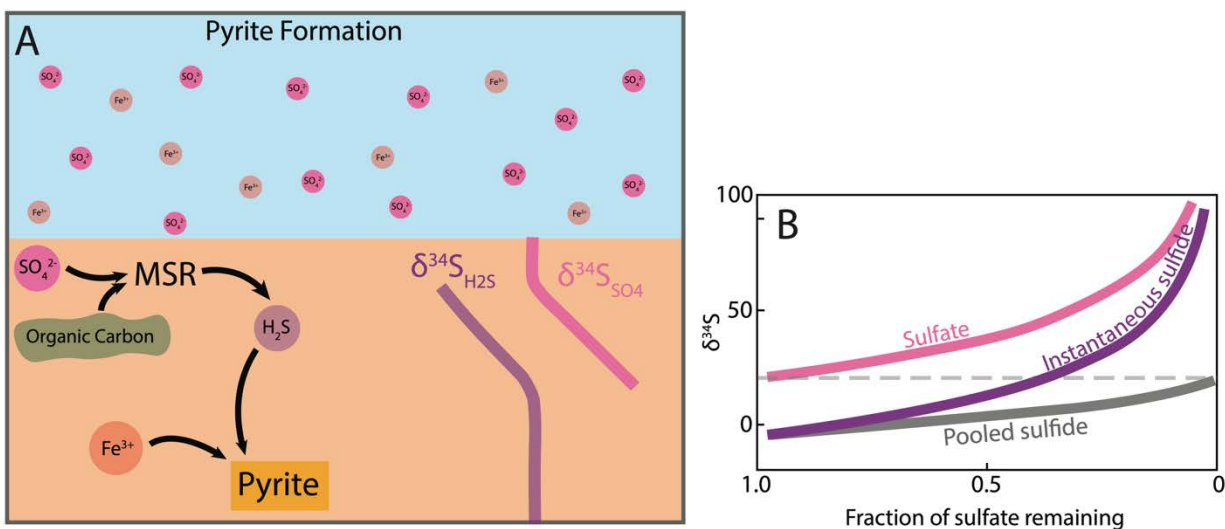
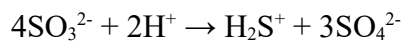


Figure 3. Metabolic pathways for the sulfur cycle modified from Fike et al., 2015. **(A)** Changing isotopic composition of H_2S (purple) and SO_4 (pink) with depth as microbial sulfate reduction (MSR) proceeds is shown. **(B)** Schematic showing the isotopic evolution of sulfate (pink), instantaneous sulfide (purple), and pooled sulfide (gray) during closed-system sulfate reduction.

Additional considerations of sulfur isotope fractionation include sulfide oxidation and disproportionation. Some isotope compositions found in the sedimentary sulfide record are more depleted in ^{34}S than can be explained by the fractionation associated with sulfate reduction alone (Canfield, 2001a). It has been proposed that these highly ^{34}S depleted sulfides result from multiple cycles of sulfide oxidation and disproportionation, which is the microbially-mediated process by which a substance is both oxidized and reduced—forming two products with the same element in different oxidation states (Canfield, 2001). Sulfide disproportionation to H_2S can result in $\delta^{34}\text{S}$ values depleted 20-37‰ relative to source sulfide, and disproportionation to sulfate can result in $\delta^{34}\text{S}$ values depleted 6-12‰ relative to source sulfide (Canfield, 2001).



Equation 4. Disproportionation of sulfite to sulfide and sulfate (Canfield, 2001).

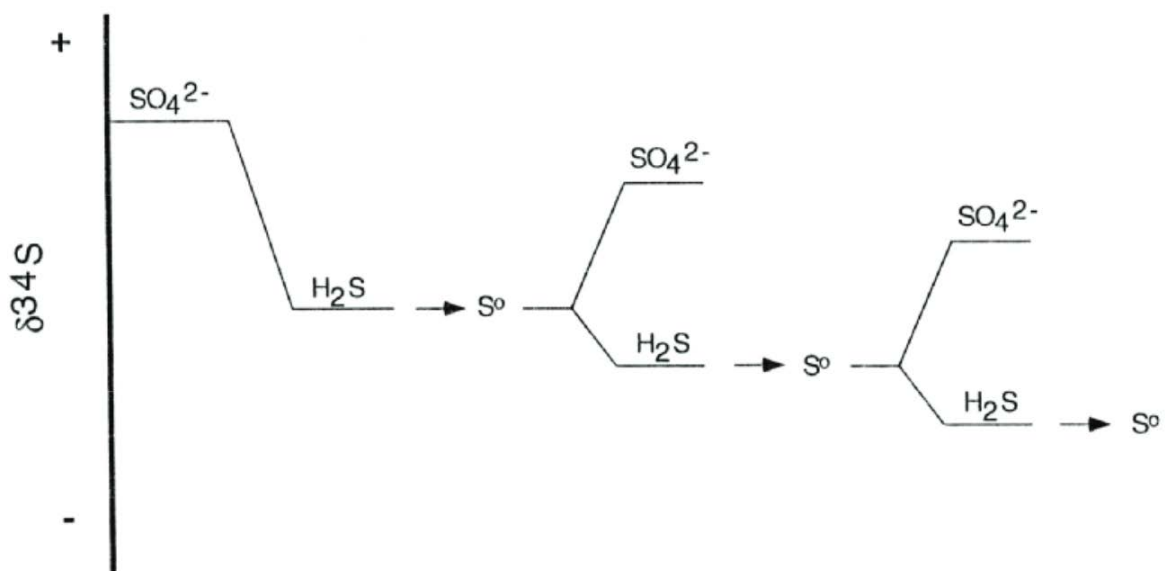


Figure 4. How the sulfur isotope composition of sedimentary sulfides can occur from cycles of oxidation and disproportionation (Canfield, 2001).

It is clear that depositional environments can shape pyrite sulfur isotope signatures that are preserved in the sedimentary record, and these records have been used to document changes in local depositional environments. Despite the influence of local conditions on pyrite $\delta^{34}\text{S}$, they have also been leveraged to reconstruct records of regional and global redox conditions; microbial activity; and biogeochemical feedback in deep time (Garrels and Lerman, 1981; Canfield and Teske, 1996; Canfield, 2004; Fakrae et al., 2024). Recently, however, questions have arisen about whether these inherently local signals can reliably be used to infer global trends, which will be explored further in the next section.

V. Inherent pyrite $\delta^{34}\text{S}$ variability

With the rise of micro-scale analytical techniques, such as secondary ionization mass spectrometry (SIMS), that allow for the isotopic analysis of individual mineral grains, there has been documentation of sulfur isotopic variability between, and within, pyrite grains of a single sample (Paiste et al., 2024; Houghton et al., 2024). These methods also allow for the evaluation of isotopic variability within populations of pyrite framboids, which is not captured by bulk $\delta^{34}\text{S}$ analysis (Bryant et al., 2023; Paiste et al., 2024; Houghton et al., 2024). Because many depositional environmental conditions can drive shifts in pyrite $\delta^{34}\text{S}$, microscale sulfur isotope analyses provide a means of investigating the major controls on these preserved signatures.

Within a single drill core, it has been documented that populations of pyrite morphology, texture, and size (framboid, $<10\mu\text{m}$ octahedral crystals, $10\text{-}20\mu\text{m}$ octahedral crystals, stratiform laminae, aggregate, etc.) can correspond to distinct sulfur isotope signatures (Paiste et al., 2024). Specifically, it has been theorized that these populations represent multiple-generations of pyrite formation during diagenesis and that only the earliest pyrite generation, represented by framboid and $<10\mu\text{m}$ octahedral crystals, records sulfur isotope values of early depositional conditions (Paiste et al., 2024).

Others have proposed that basin-wide or even global climatic conditions fundamentally control sulfide isotope compositions. For instance, some workers have interpreted glacial-interglacial cycles (Pasquier et al., 2017; Bryant et al., 2023; Halevy et al., 2023) and changes in sedimentation rate (Turchyn et al., 2009) as drivers of pyrite $\delta^{34}\text{S}$.

VI. Post-depositional alteration of sulfur records

There is evidence that in addition to early diagenetic conditions impacting pyrite $\delta^{34}\text{S}$, post-depositional processes, such as thermal alteration, can also cause the $\delta^{34}\text{S}$ values of pyrite to deviate from original depositional values (Kajiwara et al., 1981; Yamamoto, 1984; Amrani et al., 2005, 2006; Tomkins, 2010; Yallup et al., 2013; Fakhraee et al., 2024). Laboratory experiments have shown the potential for exchange between the organic sulfur and pyrite sulfur pools under thermal alteration, which can affect bulk $\delta^{34}\text{S}$ values (Amrani et al., 2005, 2006). This study simulated low temperature ($<350^\circ\text{C}$) post-depositional thermal alteration of organic sulfur-rich limestone and measured its effect on the pyrite sulfur and organic sulfur pools (Amrani et al., 2005). Under these conditions, organic sulfur displayed the potential to break down, removing a fraction of preserved sulfur from the overall preserved sulfur pool (Amrani et al., 2005). Sulfur mobilization during this process resulted in the production of H_2S gas that was significantly depleted in ^{34}S relative to the starting composition of the organic sulfur (Amrani et al., 2005). These results showed that if iron is present in the system, the thermally produced H_2S gas will readily react with it to form secondary pyrite. Like the H_2S gas, this secondary pyrite will be isotopically lighter than the initial organic sulfur composition, but isotopically heavier than the original pyrite; a 21‰ fractionation was observed between the secondary pyrite and initial organic sulfur, indicating that the addition of this secondary pyrite to the bulk pyrite sulfur pool could significantly alter the $\delta^{34}\text{S}$ of the bulk pyrite after thermal alteration (Amrani et al., 2005). In these experiments, the breakdown of organic sulfur and accumulation of secondary pyrite proceeded until 300°C . After this threshold, secondary pyrite begins to decompose, removing ^{32}S from that pool and enriching the remaining bulk pyrite in ^{34}S (Amrani et al., 2005). If all secondary pyrite is removed, the bulk pyrite composition will reflect initial, unheated values, but if not, bulk pyrite composition will be shifted.

Another factor that can cause post-depositional shifts in sulfur isotope records is reactions between metamorphic fluid and sediments at the contact between an igneous intrusion and the host rock (Tomkins, 2010; Yallup et al., 2013). When pyrite is present in the host rock, the process of desulfurization can occur, in which sulfur is liberated during the breakdown of pyrite (FeS_2) to pyrrhotite (FeS) (Eqn. 5) (Tomkins, 2010). Yallup (2013) documents sulfur concentrations of shale decrease towards a contact with a 3 m dolerite sill. In this study, sulfur in the shale takes the form of pyrite, pyrrhotite and iron sulfate within 30 cm of the contact and sulfur isotope compositions decrease towards the contact. Yallup (2013) concluded that the iron sulfates were produced during retrogressive cooling and oxidation within 20 cm of the contact. Pyrite and localized sulfur concentrations were noted in the sill, and it is proposed that this is the result of sulfur assimilation from the adjacent sediments (Yallup et al., 2013).

The kinetic isotope effect during the thermal breakdown of pyrite has been demonstrated in a laboratory experiment by Yamamoto (1984). In this experiment, pyrite was broken down in the presence of iron powder in glass tubes at 600 and 400°C. The evolution of pyrite $\delta^{34}\text{S}$ values was tracked in discrete time intervals. This study found that these values remained nearly identical to those of the initial pyrite until approximately 80% of the reaction was complete, after which the residual pyrite became appreciably enriched in ^{34}S (Yamamoto, 1984). A similar experiment tracked pyrite $\delta^{34}\text{S}$ during thermal decomposition at 600°C without added iron powder (Kajiwara et al., 1981). Under these conditions, pyrite $\delta^{34}\text{S}$ evolved according to Rayleigh fractionation, and the pyrrhotite produced was -5% relative to the starting pyrite (Kajiwara et al., 1981).

Post-depositional thermal alteration of sediments has the potential to shift sedimentary sulfur records from original depositional values via desulfurization and mixing with other sulfur pools.

The presence and extent of this shift may depend on factors such as metamorphic fluid interactions, maximum temperature, and mineral assemblage. As a result, these influences must be constrained to confidently interpret pyrite $\delta^{34}\text{S}$ in hydrothermally overprinted systems.

VII. Study Overview

It is vital to constrain the effect of post-depositional thermal alteration on the sulfur sedimentary record to properly use its signals to reconstruct depositional conditions and paleoenvironment as all sediments have undergone some heating and compaction during the lithification process. This work addresses the reliability of measured $\delta^{34}\text{S}$ values of thermally altered sediments as well as supports future studies on wider degrees of thermal alteration and potentially the development of correction models for reconstructing original $\delta^{34}\text{S}$.

The mobilization of sulfur from pyrite under thermal alteration has been demonstrated in laboratory experiments but not yet in a field setting (Amrani et al., 2005, 2006). To better understand—and potentially correct for—this process in the sedimentary rock record, its effects must first be characterized through field-based studies. This study seeks to assess how $\delta^{34}\text{S}$ records are preserved under post-depositional thermal alteration through the analysis of pyrite $\delta^{34}\text{S}$ in variably thermally altered sediments, achieved with in situ sulfur isotope analyses of $\delta^{34}\text{S}$ variation within individual pyrite grains.

The field locality is located along the eastern margin of the Raton Basin, in the northeast corner of New Mexico and features a nine m-thick mafic intrusion called the Eagle Rock Dike that is

late Oligocene to middle Miocene in age (Mark et al., 2024). Samples were collected within a single stratigraphic horizon along a transect perpendicular to the igneous intrusion within the Pierre Shale in the Raton Basin, NM.

VIII. Geologic Setting

The study locality is located within sedimentary rocks of the Raton Basin, which outcrop through present-day New Mexico and Colorado. The Raton was a structural foreland basin formed during the Laramide Orogeny in the Cretaceous (Baltz, 1965). Basin boundaries include the Sangre de Cristo uplift to the west; the Wet Mountains uplift and the Apishapa arch to the north; and the Sierra Grande arch to the east (Fig. 5) (Johnson and Wood, 1956; Dane and Bachman, 1962; Wanek et al., 1964; Baltz, 1965). The northern part of this basin was characteristically deep, while the southern part was the shallower Las Vegas sub-basin (Baltz, 1965). An intrabasinal arch, the Cimarron arch, serves as a boundary for this sub-basin (Fig. 5).

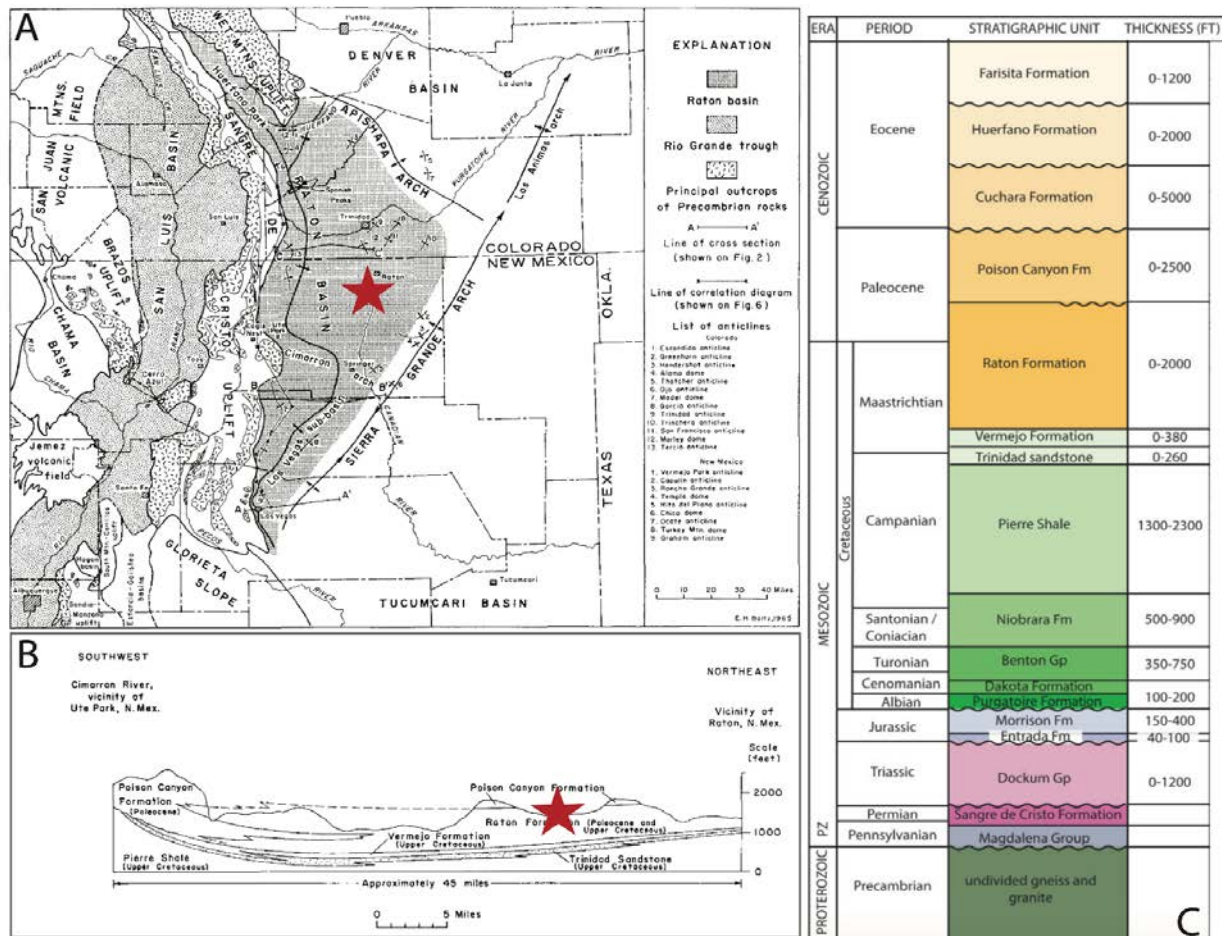


Figure 5. (A) Major tectonic elements of southeastern Colorado and northeastern New Mexico. (B) Diagram showing stratigraphic relations of uppermost Cretaceous and lower Tertiary rocks between Ute Park and Raton, New Mexico. Red star indicates approximate study location in both panels. Modified from Baltz (1965) and data from Johnson and Wood (1956), Dane and Bachmon (1962), and Wanek and others (1964). (C) Stratigraphic column showing nomenclature, thickness, and ages of the major units of the Raton Basin (Merewether et al., 2011; Bush et al., 2016).

Our study locality is within the Cretaceous (Campanian) Pierre Shale (75.77 ± 0.34 Ma) of the Raton Basin (Merewether et al., 2011). This formation was deposited in a marine environment associated with the Cretaceous Interior Seaway (Cooper et al., 2007; Berry, 2018). The Pierre Shale is primarily made up of dark gray to black, non-calcareous shale, with minor incorporation of thin beds of limestone, sandy shale, and sandstone (Johnson and Wood, 1956; Baltz, 1965). The formation has been described as up to 2,300 feet thick in the northern Raton Basin and 1,600 feet thick near the basin's southern margin (Johnson and Wood, 1956; Baltz, 1965). The Pierre Shale lies conformably atop the Niobrara Shale in much of the Raton Basin (Baltz, 1965). The upper 200-300 ft of the Pierre Shale consist of buff to gray thinly bedded, fine-grained sandstone that is interbedded with thin beds of silt and sandy shale. These sedimentary layers intertongue with the overlying Trinidad Sandstone, forming a gradational contact (Johnson and Wood, 1956).

Tertiary igneous intrusions occur as sills, dikes, and stocks within the Raton Basin (Baltz, 1965). Mafic and ultramafic intrusions have been noted throughout the basin, associated with extensional deformation caused by the Rio Grande Rift (Baltz, 1965).

Materials and Methods

I. Sample collection and preparation

Samples were collected at an outcrop ($36^{\circ}39'53.8''\text{N}$ $104^{\circ}29'41.4''\text{W}$) of the Pierre Shale in the Raton Basin, NM. Forty-eight samples were collected on the decimeter to meter scale interval within a single bed with increasing distance from the igneous intrusion, for a total distance of 22 m from the dike. Sampling for the transect was completed within a single stratigraphic horizon, cut orthogonally by the dike, to minimize potential $\delta^{34}\text{S}$ heterogeneity.

After obtaining the samples, each one was cleaned and powdered. Oxidized portions of samples were removed from the material prior to powdering using a water-cooled rock-saw or a rotary drill. Fissile whole-rock samples were powdered using a mortar and pestle, while material from well-consolidated whole-rock samples was extracted with a rotary drill.

		Analyses				
Sample ID	Distance from Dike (m)	Secondary ion mass spectrometer (SIMS)	Scanning electron microscopy (SEM)	Acid insoluble sulfur and organic carbon analysis	Bulk total carbon and sulfur analysis	X-ray diffraction (XRD)
24-150	0.50	x	x	x	x	x
24-152	1.50				x	
24-154	2.50	x	x	x	x	
24-155	3.00			x		
24-157	4.00			x	x	
24-160	5.00			x	x	
24-161	5.25	x	x	x	x	
24-162	5.50			x		
24-164	6.00	x	x	x	x	x
24-170	7.50	x	x	x	x	

24-175	8.75	x	x	x	x	
24-181	10.50			x	x	
24-183	11.00			x	x	
24-185	12.00			x	x	
24-187	14.00			x	x	
24-189	16.00			x	x	
24-190	17.00			x		
24-191	18.00	x	x	x	x	x
24-192	19.00			x		
24-193	20.00	x		x		
24-195	22.00		x	x		

Table 1. Samples collected and analysis methods used in this study.

II. Acid insoluble carbon and sulfur content

Fifteen samples were decarbonated and analyzed for acid insoluble carbon (total organic carbon, or TOC) and sulfur contents. To prepare each sample for analysis, ~0.2 g of sample powder was decarbonated in 2 M HCl, removing inorganic carbon, Ca-sulfate, and carbonate-associated sulfate contents in the sample. Weight percent (wt%) acid-soluble content was calculated by subtracting the ending (decarbonated) sample mass by the starting sample mass and dividing by the starting sample mass. Following decarbonation, the samples were rinsed with deionized H₂O

and centrifuged for 5 minutes at 400 rpm and tested for pH. These steps were repeated until a neutral pH was reached. Samples were then dried in an oven at $\sim 40^{\circ}\text{C}$ for ~ 48 hours. The weight of the sample is recorded after this procedure to determine the percent carbonate content. Each sample was homogenized with a mortar and pestle before ~ 100 g was loaded into ceramic boats for analysis. The residues are analyzed for acid insoluble contents using a benchtop Eltra Elemental Analyzer, using carbon and sulfur in ore standard material. The precision determined by commercial standards was 0.024% for carbon and 0.038% for sulfur and error (2σ) was determined to be 0.145 wt% for the acid insoluble contents based on duplicate measurements.

III. Bulk sulfur and carbon content

Fifteen samples were analyzed for total sulfur and carbon contents. ~ 100 g of sample powder was loaded into ceramic boats for analysis using a benchtop Eltra Elemental Analyzer and a carbon and sulfur in ore standard material. The precision determined by commercial standards was 0.024% for carbon and 0.038% for sulfur. Error (2σ) was determined to be 0.003 wt% for the bulk sulfur and carbon contents based on duplicate measurements.

IV. Mineralogy

Three X-ray diffraction (XRD) analyses were carried out using a Rigaku Rapid II X-ray diffraction system with Mo Ka radiation and ~ 100 μm beam size. Individual thin layers were selected from the attached camera in the Rigaku system. Diffraction data were collected using a 2-D image-plate detector, integrated through the Rigaku's 2DP software, and formulated into traditional 2θ vs. intensity patterns. Phase identification and unit-cell refinement were done using Jade 9 software (Fang and Xu, 2019).

V. Sulfide grain characterization

8 samples were analyzed using a Hitachi S3400 Variable Pressure Scanning Electron Microscope (SEM) in order to characterize pyrite grains within each sample, as well as select pyrite grains for in situ sulfur isotope analysis. To prepare samples for SEM analysis, rock chips from each sample were mounted in a 2.5 cm diameter and 5 mm thick epoxy disk (Williford et al., 2011). Two epoxy mounts were made, each containing 4 samples (Fig. 6). Epoxy disks were polished with diamond paste until a maximum surface relief of $\sim 1 \mu\text{m}$ was observed and then mounts were cleaned in a sonicator (Kita et al., 2009). Preliminary imaging was completed under a reflected light microscope. A carbon coat of $\sim 30\text{-}40 \mu\text{m}$ was applied to the surface of the mount.

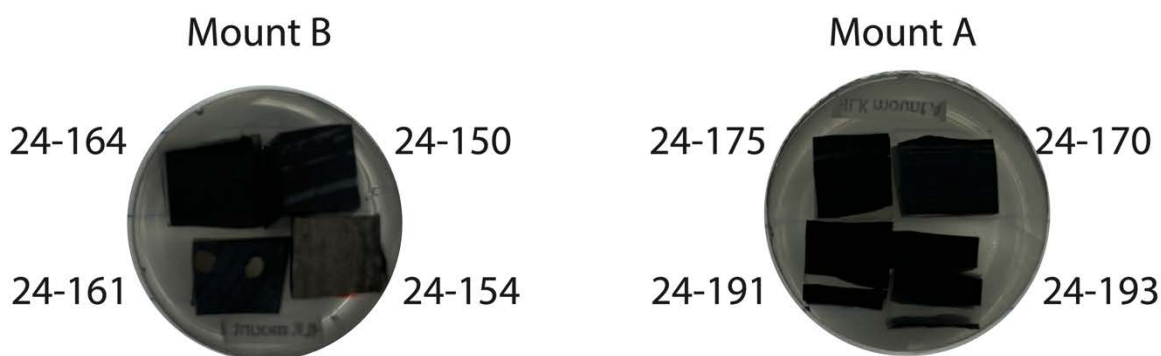


Figure 6. Epoxy mounts for SEM and SIMS analysis.

Pyrite grains within each sample were identified and characterized using backscatter electron (BSE) imaging, secondary electron (SE) imaging, as well as analyzed for mineral spectra using energy dispersive spectroscopy (EDS). This was completed under 15.0 kV conditions on the SEM.

To characterize the pyrite grains within each sample, grains were first identified visually using BSE imaging and SE imaging. Grain shape, texture, and appearance in BSE and SE imaging was

assessed in visual identification (Cui et al., 2018; Bryant et al., 2020). If the mineral phase was unclear, the mineral spectra was assessed using energy dispersive spectroscopy (EDS). After initial pyrite identification, grains were screened for suitability for SIMS analysis by size.

Grains that were both identified as pyrite and as a suitable target for SIMS analysis, BSE and SE images of individual grains were captured and grains were characterized in terms of morphology and size distributions. Grain size was assessed by average diameter in microns (μm).

Morphology was assessed by grain texture and shape. All pyrite grains fell into one of the following morphology categories: (i) framboid, (ii) recrystallized framboid, (iii) crystal, or (iv) irregular crystal (Cui et al., 2018; Bryant et al., 2020). Framboid grain morphology is defined by its spheroidal to sub-spheroidal shape and presence of visually and texturally distinct equimorphic microcrystals clustered to form the grain (Cui et al., 2018; Bryant et al., 2020).

Recrystallized framboids are defined as cemented pyrite aggregates, in which microcrystals are difficult to discern due to pyritic cementations (Cui et al., 2018; Bryant et al., 2020). The crystal pyrite morphology is defined by its spheroidal to sub-spheroidal shape and homogenous internal texture (Cui et al., 2018). Irregular crystals are defined by their irregular shape and heterogenous texture, often featuring inclusions within the grain.

Additionally, each epoxy mount underwent raster imaging, capturing BSE and SE images across the entire surface. The reflected light images and all BSE and SE images were compiled and geospatially referenced in a QGIS file. These QGIS files were used to plan in situ sulfur isotope analysis spots and navigate the grain mounts during that analysis, as well as for point counting to assess pyrite grain abundance, morphology distribution, and grain size distribution within each sample.

VI. In situ sulfur isotope analysis

8 samples were selected for in situ sulfur isotope analyses within individual pyrite grains using a secondary ion mass spectrometer (SIMS). These samples represent varying distances away from the igneous intrusion. Rock chip mounts, described above, were made in preparation for this analysis. The pyrite standard UWPY-1 was mounted in the center of each disk (Fig. 6). The mount retained the carbon coat of ~30-40 μm , applied for SEM analysis, for charge compensation on the SIMS (Ushikubo et al., 2014; Cui et al., 2018).

147 spots were analyzed for sulfur isotope composition using a CAMECA ims-1280 large radius multi-collector ion microprobe at the WiscSIMS Lab, Department of Geosciences, University of Wisconsin—Madison. ^{32}S and ^{34}S were measured simultaneously by multicollector with a ~3 μm diameter $^{133}\text{Cs}^+$ primary ion beam with a 30-pA current (Cui et al., 2018). Each analysis included a 60 s pre-sputter, followed by centering of the secondary beam in the field aperture, and then 20 counting cycles of 4 s each (80 s total of counting time).

The WiscSIMS Lab internal pyrite standard UWPY-1 (Balmat Mine, New York, $\delta^{34}\text{S} = 16.04 \pm 0.18\text{‰}$, $\Delta^{34}\text{S} = -0.003 \pm 0.009 \text{‰}$, 2SD, V-CDT) was used to calibrate these analyses (Ushikubo et al., 2014). Data quality was evaluated using parameters collected during SIMS analysis, including the $^{32}\text{SH}/^{32}\text{H}$ ratio, relative secondary ion yield, and standard error—and further assessed through post-analysis pit imaging.

Intragranular variability for each grain was calculated using sample variance (Eqn. 6) for multiple analysis spots on a single sulfide grain.

$$s^2 = \frac{\sum_{t=1}^n (x_i - \bar{x})^2}{n-1}$$

Equation 6. Sample variance (s^2).

Results

I. Thermal maturity constraints

A. Carbon content and acid soluble content

Bulk and acid insoluble carbon content (total organic carbon, or TOC), both decrease with decreasing sampling distance from the igneous intrusion, while acid soluble contents increase slightly with decreasing sampling distance from the igneous intrusion (Fig. 7).

Acid soluble contents range from 0.14 wt% in sample 24-170 (7.5 m) to 0.31 wt% in sample 24-150 (0.5 m) (Fig. 7). Bulk carbon contents vary between 0.06 wt% in sample 24-150 (0.5 m) and 2.60 wt% in sample 24-193 (20 m) (Fig. 7). TOC content within the sampled bed is between 0.07 and 1.67 wt%, generally decreasing with decreasing sampling distance from the igneous intrusion (Fig. 7). Sample 24-181 (10.5 m) has the highest TOC value of 1.67 wt% and sample 24-155 (3 m) has the lowest TOC value of 0.07 wt%.

Between 10-20 m sampling distance from the igneous intrusion, acid soluble content averages 0.21 wt%, bulk carbon content averages 2.29 wt%, and TOC content averages 1.53 wt% (Fig. 7).

Between 2-10 m sampling distance from the igneous intrusion, acid soluble content averages 0.18 wt%, bulk carbon content averages 0.61 wt%, and TOC content averages 0.57 wt% (Fig. 7).

Between 0-2 m sampling distance from the igneous intrusion, acid soluble content averages 0.31 wt%, bulk carbon content averages 0.06 wt%, and TOC content averages 0.10 wt% (Fig. 7).

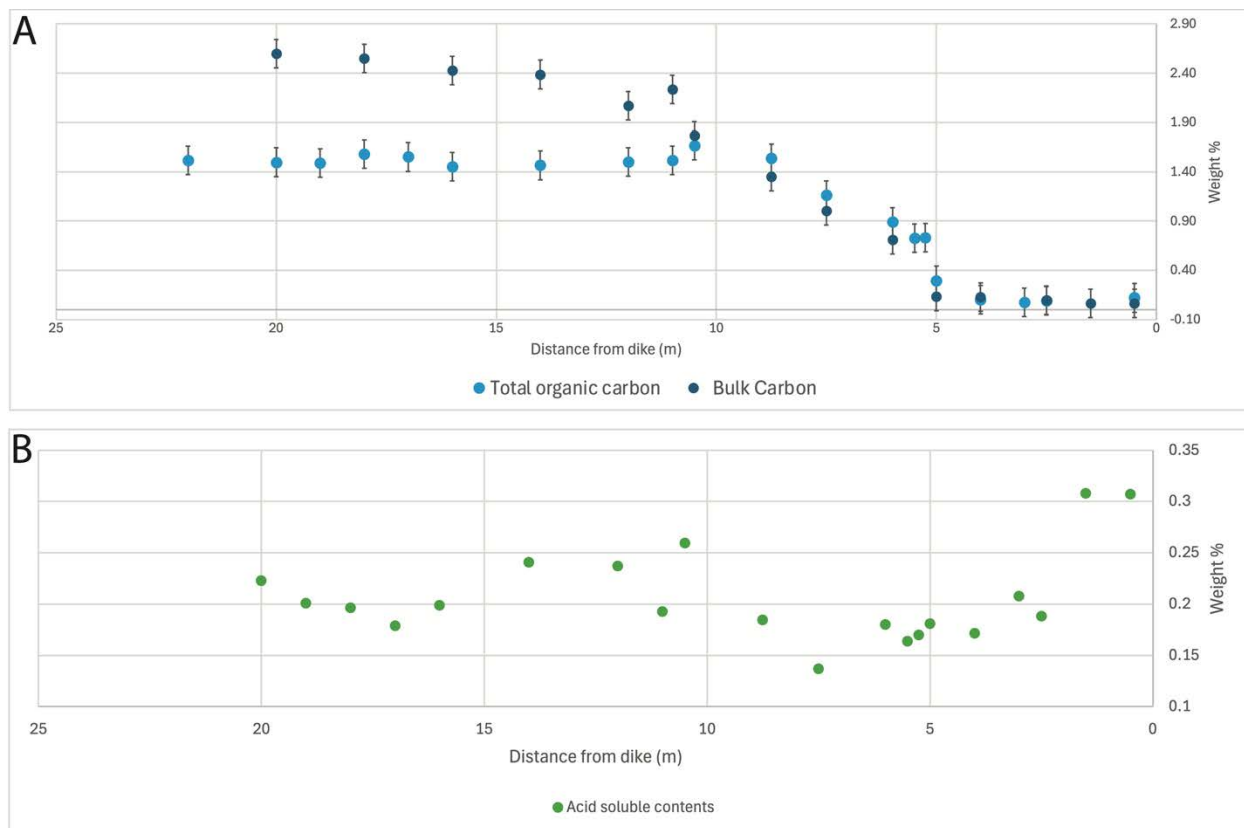


Figure 7. (A) Bulk carbon contents and total organic carbon (TOC) contents with distance from the dike; average error (2σ) is 0.15 and 0.003 wt% for total organic carbon data and bulk carbon data, respectively. **(B)** Acid-soluble contents with distance from the dike.

B. Sulfur content

Bulk sulfur contents and acid insoluble sulfur contents generally increase with decreasing sampling distance from the igneous intrusion (Fig. 8). Bulk sulfur contents vary between 0.18 wt% (24-185, 12 m) and 1.34 wt% (24-150, 0.5 m) (Fig. 8). Acid insoluble sulfur contents vary between 0.1 wt% (24-161, 5.25 m) and 0.72 wt% (24-170, 7.5 m) (Fig. 8).

Between 10-20 m sampling distance from the igneous intrusion, bulk sulfur content averages 0.58 wt%, and acid insoluble sulfur content averages 0.29 wt% (Fig. 8). Between 2-10 m

sampling distance from the igneous intrusion, bulk sulfur content averages 0.86 wt%, and acid insoluble sulfur content averages 0.35 wt% (Fig. 8). Between 0-2 m sampling distance from the igneous intrusion, bulk sulfur content averages 1.22 wt%, and acid insoluble sulfur content averages 0.56 wt% (Fig. 8).

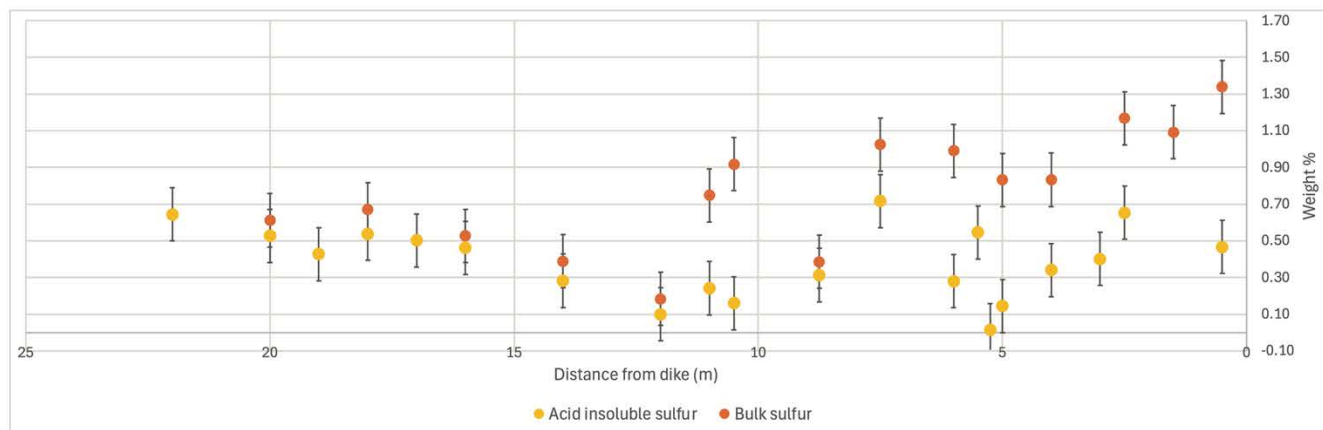


Figure 8. Bulk sulfur contents and acid insoluble sulfur contents with distance from the dike; average error (2σ) is 0.15 and 0.003 wt% for acid insoluble sulfur data and bulk sulfur data, respectively.

C. Mineralogy

The mineralogy of sample 24-150 (0.5 m) is 69.17% quartz, 30.34% albite, and 0.5% chlorite (Fig. 9). Sample 24-164 (6 m) contains 72.20% albite, 17.64% quartz, and 10.15% chlorite (Fig. 9). Sample 24-191 (18 m) contains 28.36% albite, 30.01% quartz, 7.53% kaolinite, 33.74% illite, and 0.37% chlorite (Fig. 9).

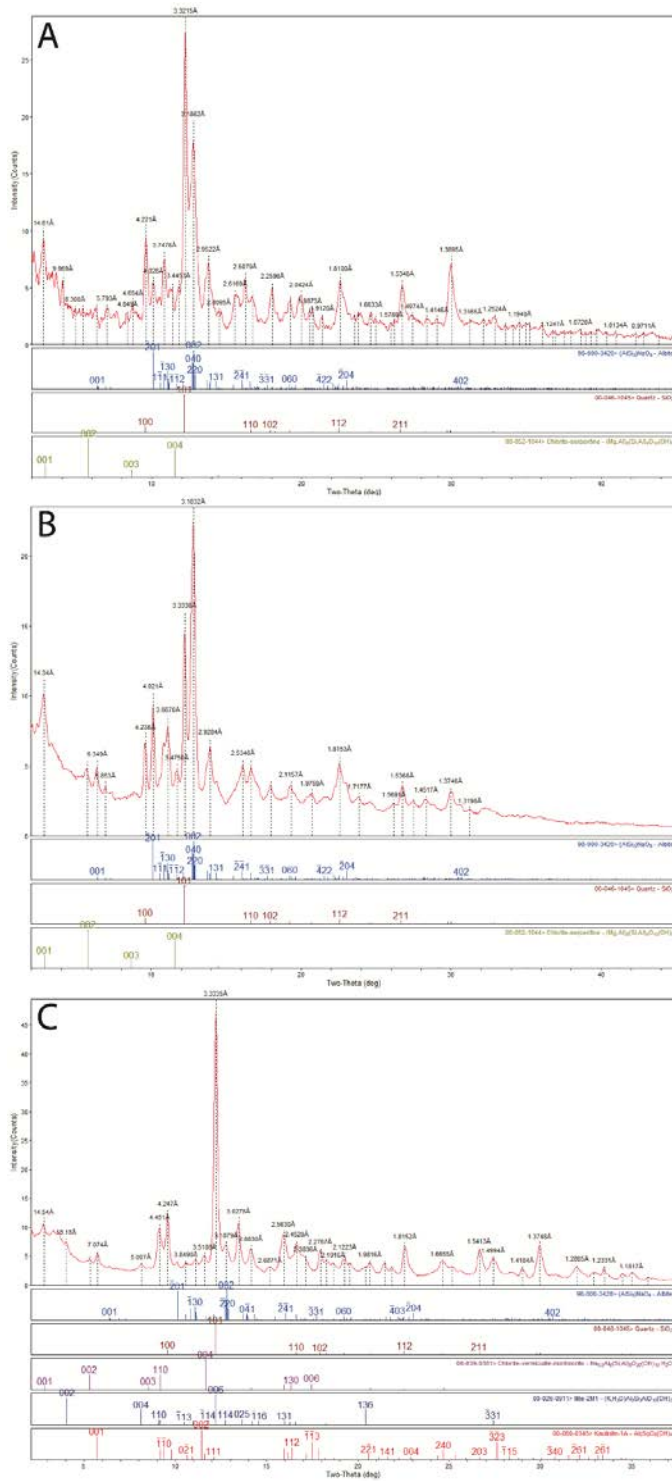


Figure 9. (A) Mineralogy of sample 24-150 (0.5 m). (B) Mineralogy of sample 24-164 (6 m). (C) Mineralogy of sample 24-191 (18 m).

II. Sulfide grain characterization

Within each sample, sulfide grains were characterized in terms of morphology and size distributions (Fig. 10).

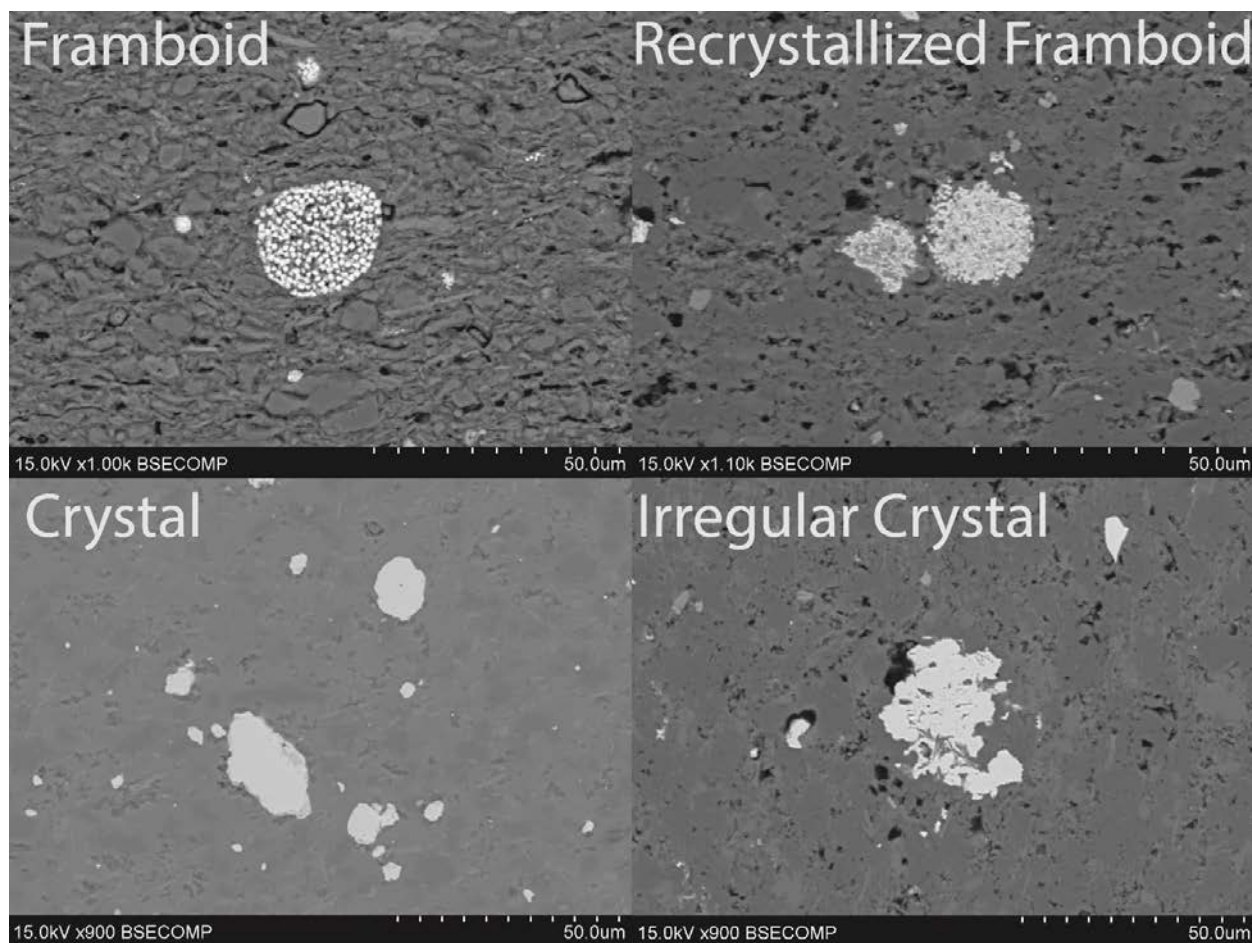


Figure 10. Framboid (24-193), recrystallized frambooid (24-170), crystal, (24-150) and irregular crystal (24-154) sulfide grain morphologies in the Pierre Shale.

In sample 24-150, sulfide grain diameters range from 0.5-34 μm . 99% of sulfide grains have diameters less than 14 μm , and 1% are 14-34 μm . 95% of sulfide grains are crystal and 5% are

irregular crystal (Fig. 11). SEM imaging of the matrix displays interlocking quartz-albite dominated texture and limited pore space in this sample (Fig. 11).

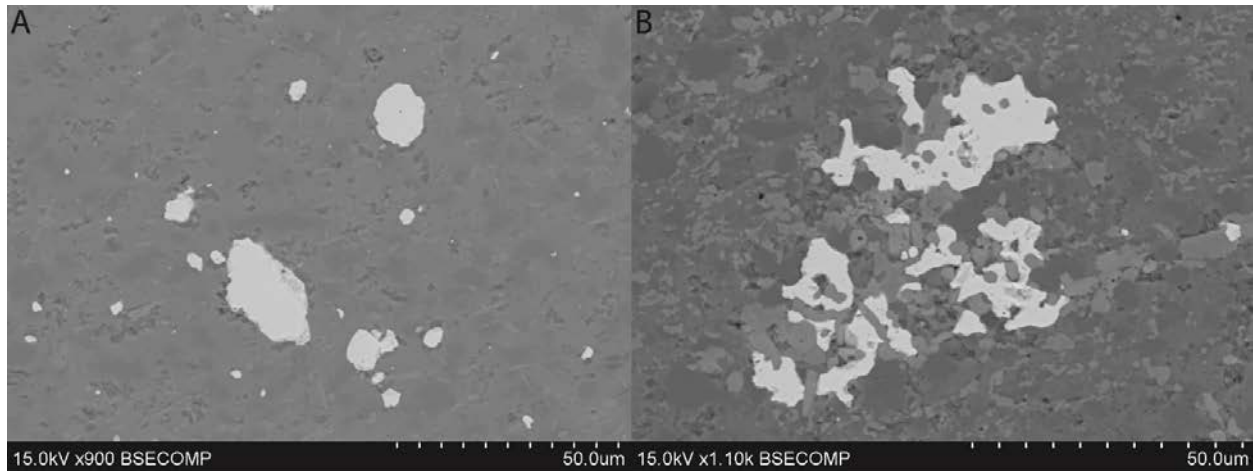


Figure 11. BSE images of sulfide grains in sample 24-150 **(A)** Grains displaying crystal morphology from sample 24-150. **(B)** Grains displaying irregular crystal morphology from sample 24-150.

In sample 24-154, sulfide grain diameters range from 0.5-54 μm . 98% of sulfide grains have diameters less than 14 μm , 1% have 14-34 μm diameters, and 1% have 35-54 μm diameters. 95% of sulfide grains display a crystal morphology and 5% display an irregular crystal morphology (Fig. 12). SEM imaging of the matrix displays moderate pore space in this sample (Fig. 12).

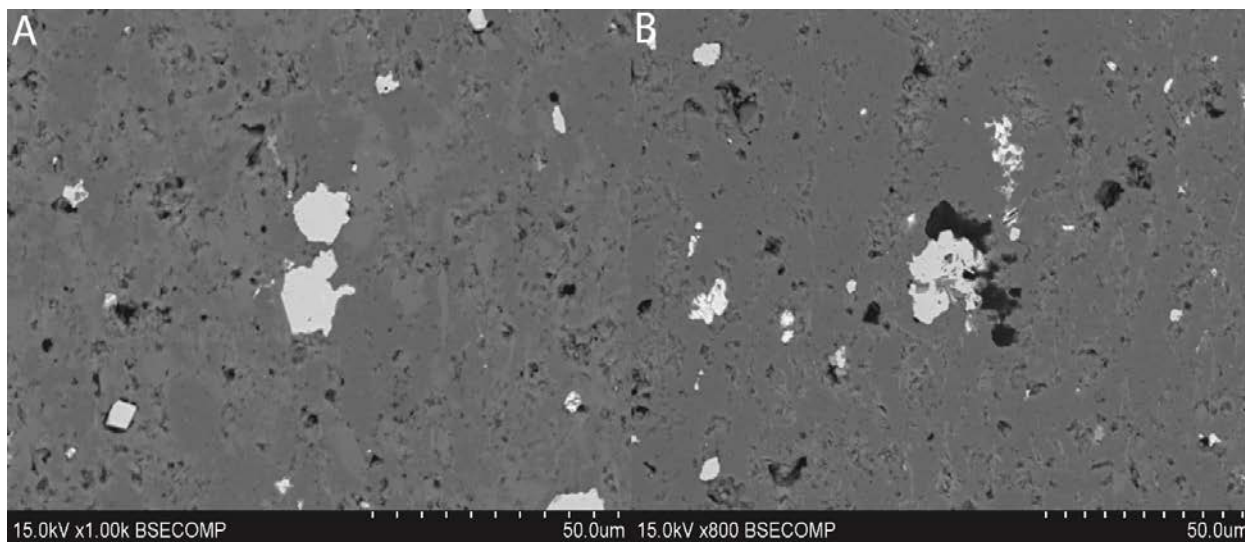


Figure 12. BSE images of sulfide grains in sample 24-154. **(A)** Grains displaying crystal morphology from sample 24-154. **(B)** Grains displaying irregular crystal morphology from sample 24-154.

Sulfide grains in sample 24-161 range in diameter from 0.5-2000 μm and display only crystal morphology. This sample has characteristically massive sulfide crystals, 1000-2000 μm in diameter (Fig. 13A). In the matrix surrounding these massive crystals, small crystals less than 14 μm are present but sparse (Fig. 13B). SEM imaging of the matrix displays moderate pore space in this sample (Fig. 13B).

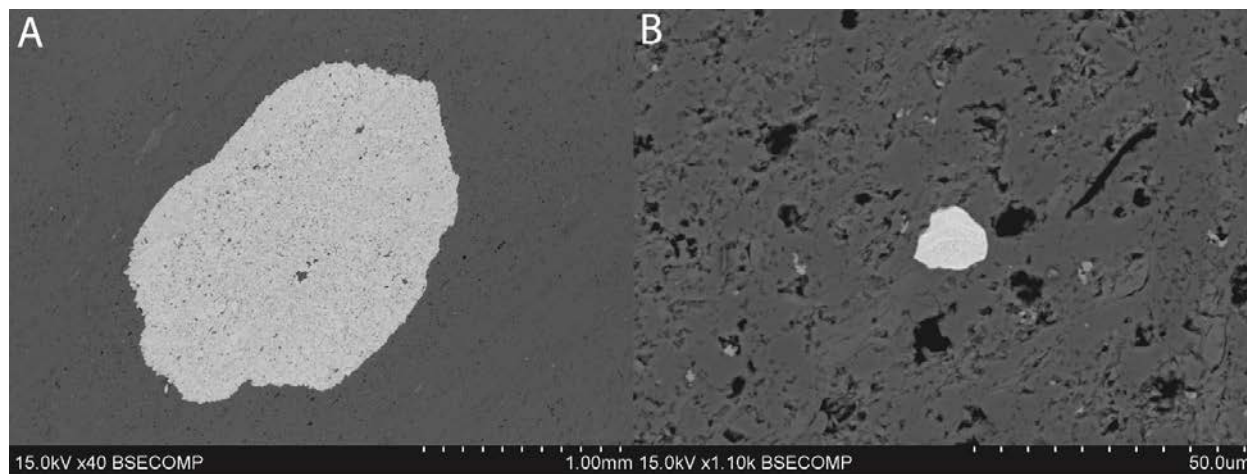


Figure 13. BSE images of sulfide grains in sample 24-161. **(A)** Massive sulfide crystal from sample 24-161. **(B)** Grain displaying a crystal morphology from sample 24-161.

Sulfide grains in sample 24-164 range in diameter from 0.5-54 μm and display crystal, irregular crystal, framboid, or recrystallized framboid morphology. 88% of sulfide grains have diameters less than 14 μm , 11% have 14-34 μm diameters, and 1% have 35-54 μm diameters. 40% of sulfide grains display a crystal morphology, 40% display an irregular crystal morphology, 5% display a framboid morphology, and 15% display a recrystallized framboid morphology (Fig. 14). 99% of sulfide grains from sample 24-164 display Fe-oxide rims and significant replacement by Fe-oxide minerals (Fig. 14). SEM imaging of the matrix displays moderate pore space in this sample (Fig. 14).

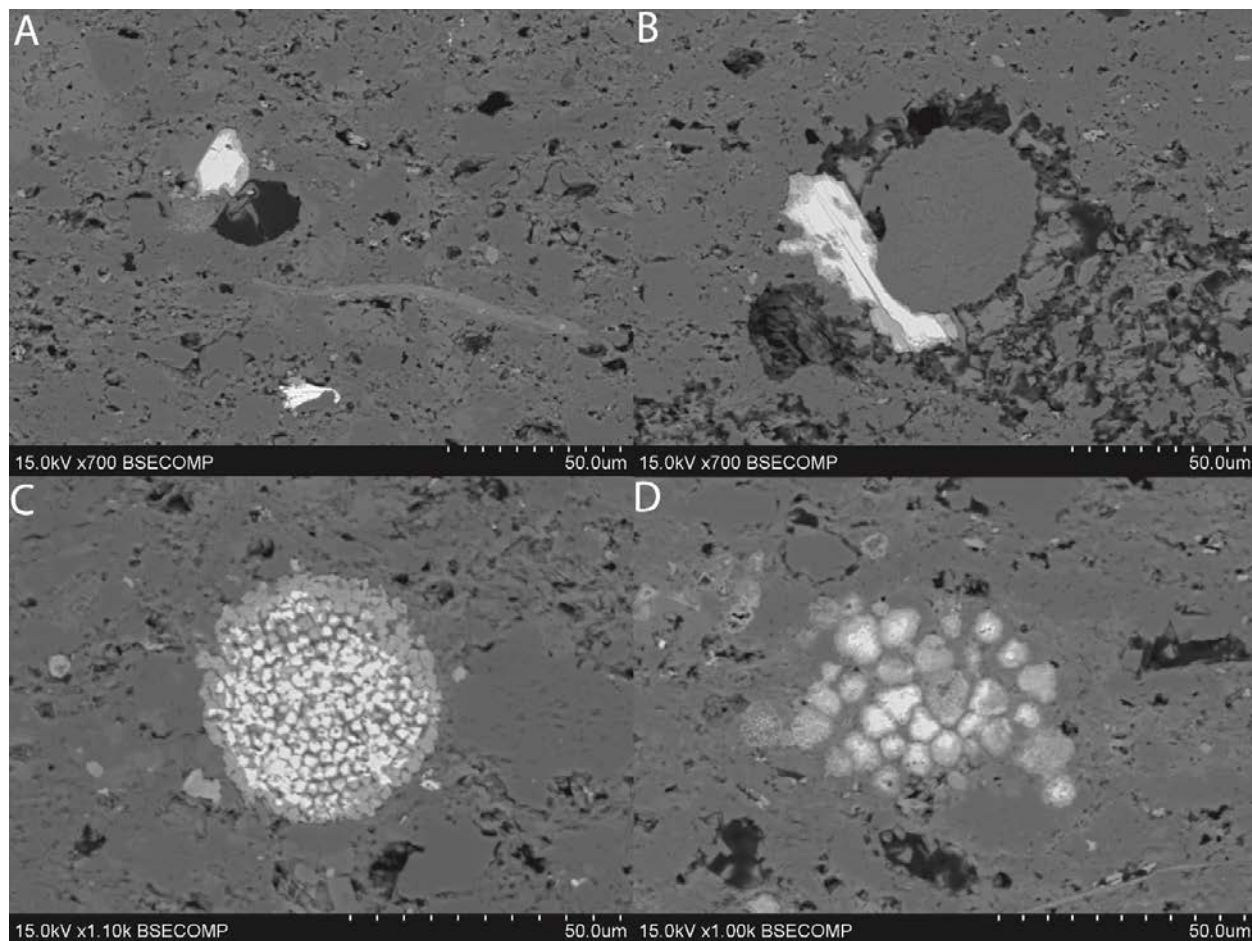


Figure 14. BSE images of sulfide grains in sample 24-164. **(A)** Crystal sulfide grain with Fe-oxide rim from sample 24-164. **(B)** Irregular crystal with Fe-oxide rim from sample 24-164. **(C)** Framboid with Fe-oxide rim and Fe-oxide replacement from sample 24-164. **(D)** Recrystallized framboids with Fe-oxide rims from sample 24-164.

Sulfide grains in sample 24-170 range in diameter from 0.5-80 μm and display crystal, irregular crystal, framboid, or recrystallized framboid morphology. 87% of sulfide grains have diameters less than 14 μm , 10% have 14-34 μm diameters, 2% have 35-54 μm diameters, 1% have 55-80 μm diameters. 11% of sulfide grains display a crystal morphology, 6% display an irregular crystal morphology, 77% display a framboid morphology, and 6% display a recrystallized

framboid morphology (Fig. 15). Framboid grains in this sample are often clustered into oblong aggregates (Fig. 15C). SEM imaging of the matrix displays clay minerals and pore space in this sample (Fig. 15).

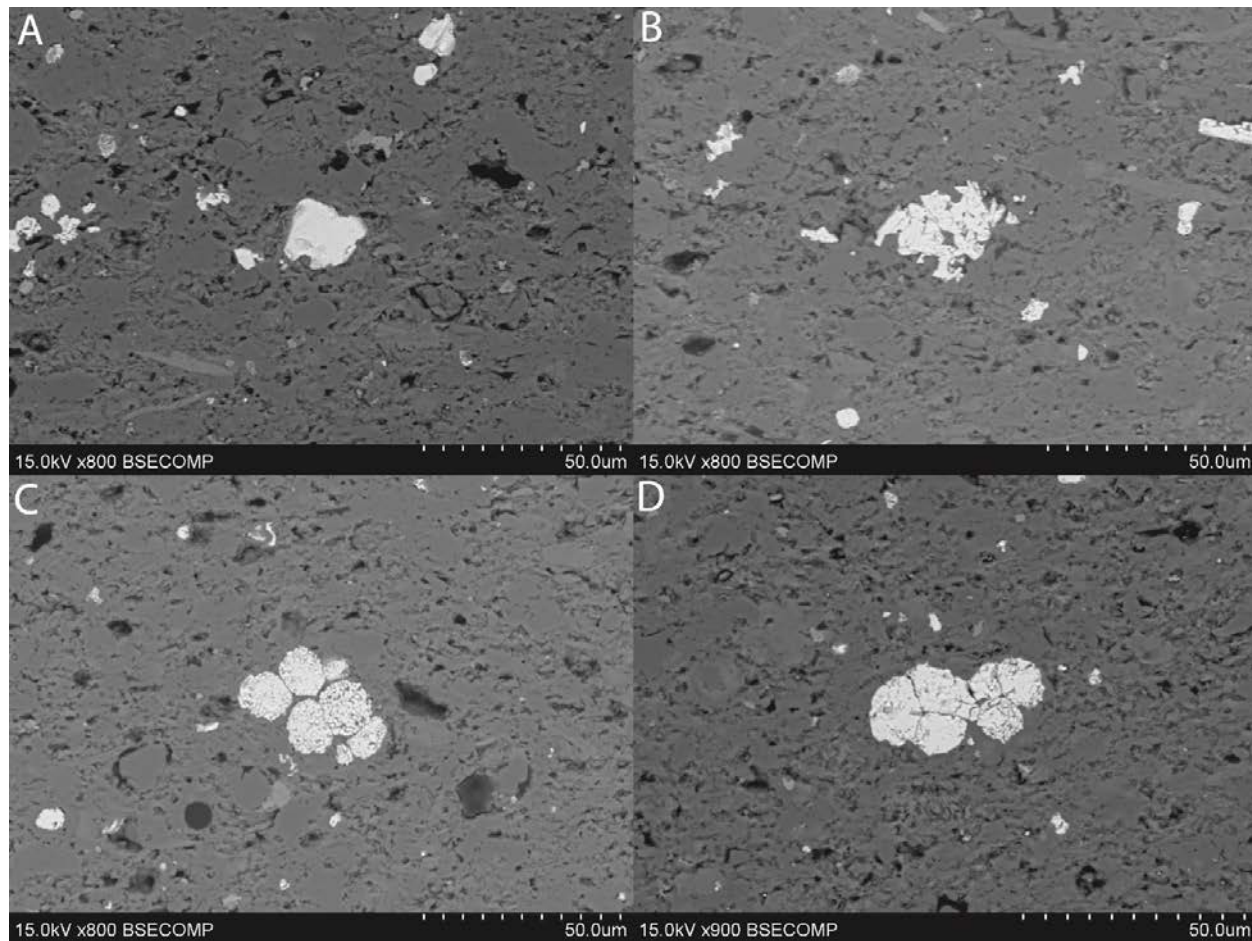


Figure 15. BSE images of sulfide grains in sample 24-170. **(A)** Grain displaying a crystal morphology from sample 24-170. **(B)** Grain displaying an irregular crystal morphology from sample 24-170. **(C)** Cluster of framboids from sample 24-170. **(D)** Grains displaying recrystallized framboid morphology from sample 24-170.

Sulfide grains in sample 24-175 range in diameter from 0.5-34 μm and display crystal, irregular crystal, framboid, or recrystallized framboid morphology. 70% of sulfide grains have diameters less than 14 μm , 30% have 14-34 μm diameters. 3% of sulfide grains display a crystal morphology, 6% display an irregular crystal morphology, 10% display a framboid morphology, and 81% display a recrystallized framboid morphology (Fig. 16). 99% of sulfide grains from sample 24-164 display Fe-oxide rims and significant replacement by Fe-oxide minerals (Fig. 16). SEM imaging of the matrix displays clay minerals and pore space in this sample (Fig. 16).

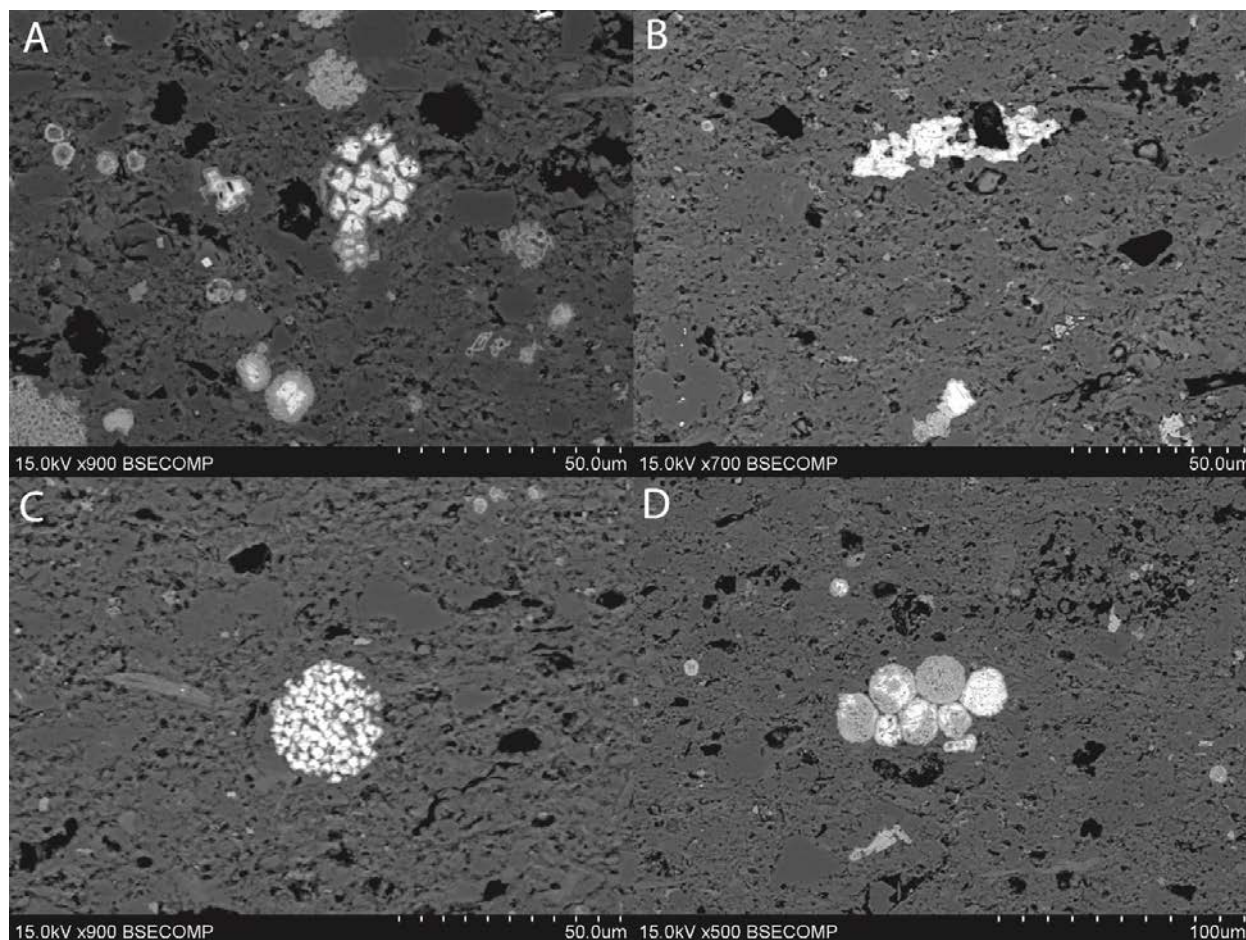


Figure 16. BSE images of sulfide grains in sample 24-175. (A) A cluster of crystals with Fe-oxide rim from sample 24-175. (B) Irregular crystal with Fe-oxide rim from sample 24-175. (C)

Framboid with Fe-oxide rim from sample 24-175. **(D)** A cluster of recrystallized framboids from sample 24-175 with Fe-oxide rims and Fe-oxide replacement.

Sulfide grains in sample 24-191 range in diameter from 0.5-54 μm and display irregular crystal, framboid, or recrystallized framboid morphology (Fig. 17). 95% of sulfide grains have diameters less than 14 μm , 5% have 14-34 μm diameters, and >1% have 35-54 μm diameters. 1% of sulfides display an irregular crystal morphology, 87% display a framboid morphology, and 12% display a recrystallized framboid morphology (Fig. 17). SEM imaging of the matrix displays clay minerals and pore space in this sample (Fig. 17).

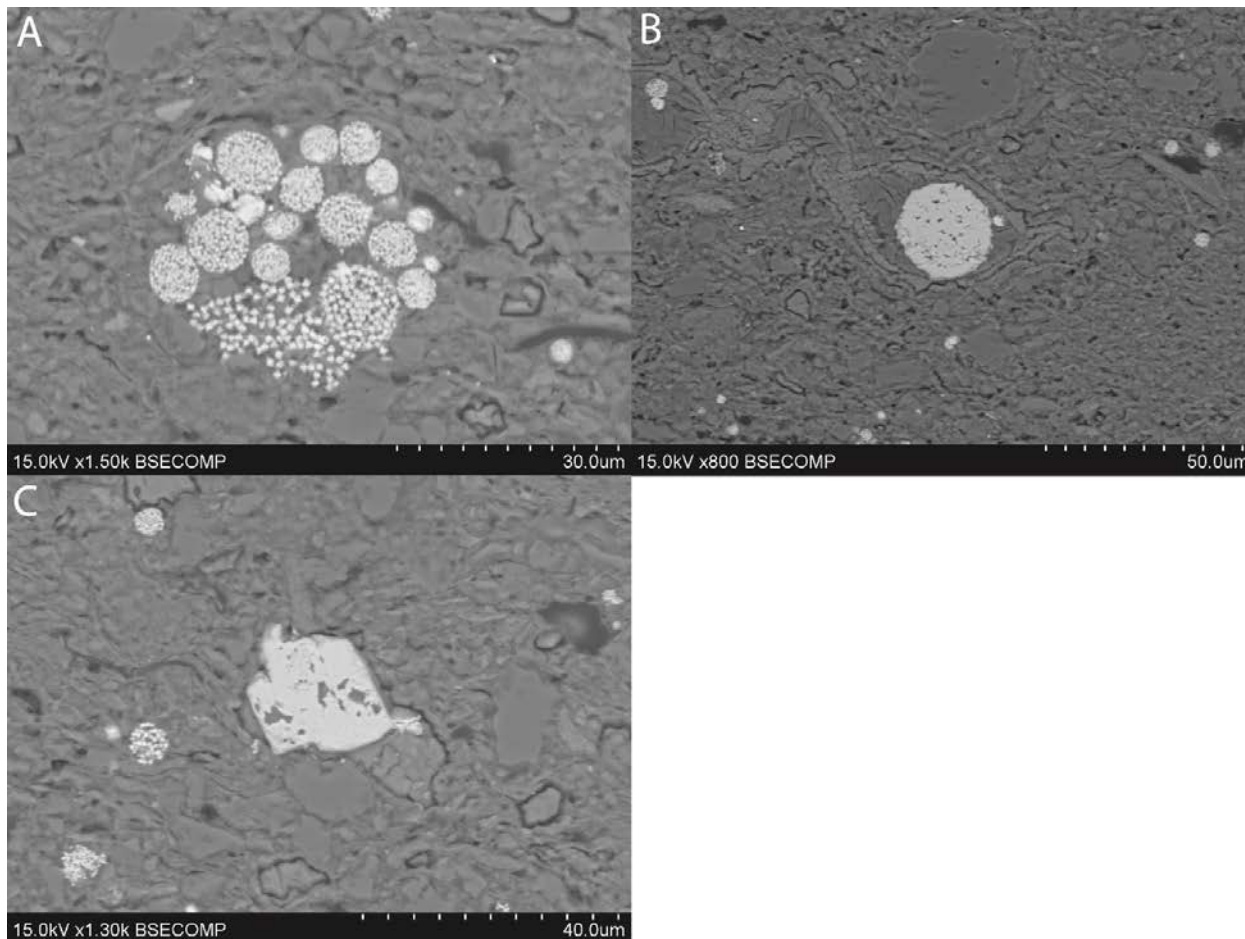


Figure 17. BSE images of sulfide grains in sample 24-191. **(A)** Cluster of framboids from sample 24-191. **(B)** Recrystallized framboid from sample 24-191. **(C)** Irregular crystal from sample 24-191.

Sulfide grains in sample 24-193 range in diameter from 0.5-34 μm and display crystal, framboid, or recrystallized framboid morphology (Fig. 18). 95% of sulfide grains have diameters less than 14 μm and 5% have 14-34 μm diameters 1% of sulfide display a crystal morphology, 92% display a framboid morphology, and 8% display a recrystallized framboid morphology (Fig. 18). SEM imaging of the matrix displays sedimentary grain texture, clay minerals, and pore space in this sample (Fig. 18).

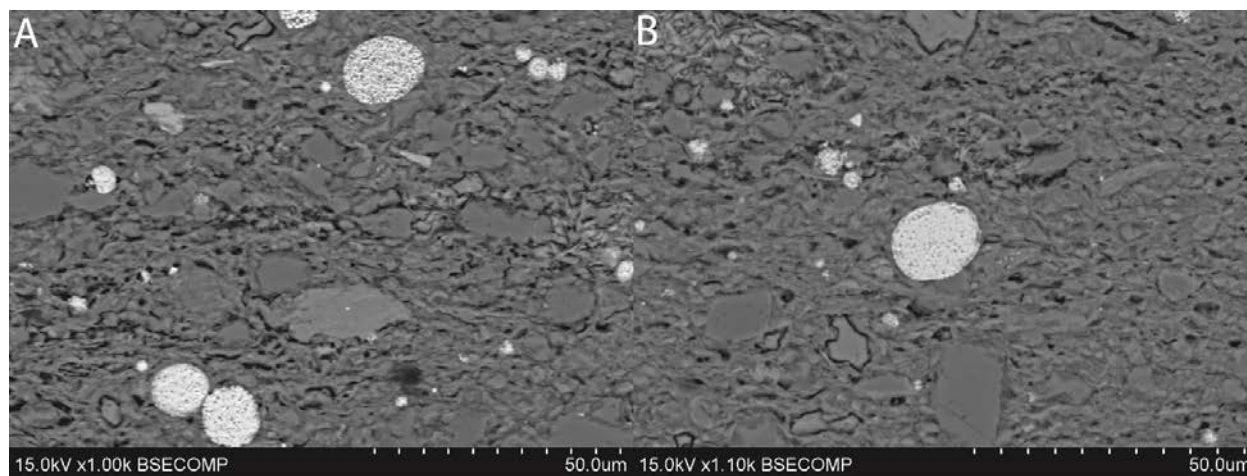


Figure 18. BSE images of sulfide grains in sample 24-193. **(A)** Framboids and $>14 \mu\text{m}$ crystals from sample 24-193. **(B)** Recrystallized framboid and a $>14 \mu\text{m}$ crystals from sample 24-193.

III. In situ sulfur isotope analyses

A. Inter-grain $\delta^{34}\text{S}$ variability

After standard post-SIMS screening for data quality, 109 analysis spots were retained for interpretation. $\delta^{34}\text{S}$ values obtained using SIMS reflect the sulfur isotope composition of the $\sim 3\mu\text{m}$ diameter analysis spot on a single sulfide grain (Fig. 19A). Sulfide $\delta^{34}\text{S}$ values in this section are reported ± 2 standard deviation (2σ). All analyses are reported in per mille notation relative to Vienna Canyon Diablo Troilite (VCDT), which has a $^{34}\text{S}/^{32}\text{S}$ ratio of 1/22.6436 (Ding et al., 2001). Within the sample 24-193 (20 m), $\delta^{34}\text{S}$ values range from $-44.85 \pm 0.47\text{‰}$ to $-29.50 \pm 0.47\text{‰}$ (range=15.35‰), have an average value of -35.47‰ (n=16), and a median value of -34.41‰ (n=16) (Fig. 19A).

Sulfide $\delta^{34}\text{S}$ values in sample 24-191 (18 m) range from $-45.80 \pm 0.68\text{‰}$ to $14.77 \pm 0.68\text{‰}$ (range=31.02‰), have an average value of -33.11‰ (n=22), and a median value of -33.89‰ (n=22) (Fig. 19A).

Sulfide $\delta^{34}\text{S}$ values collected from sample 24-175 (8.75 m) range from $-39.35 \pm 0.49\text{‰}$ to $-27.44 \pm 0.49\text{‰}$ (range=11.91‰). Sulfide $\delta^{34}\text{S}$ values average -34.00‰ (n=8) and have a median value of -34.46‰ (n=8) (Fig. 19A).

Sulfide $\delta^{34}\text{S}$ values collected from sample 24-170 (7.5 m) have a minimum $\delta^{34}\text{S}$ value of $-39.28 \pm 0.47\text{‰}$ and a maximum value of $-20.08 \pm 0.49\text{‰}$ (range=19.21‰). Sulfide $\delta^{34}\text{S}$ has an average value of -32.77‰ (n=14) and a median value of -33.34‰ (n=14) (Fig. 19A).

Sulfide $\delta^{34}\text{S}$ values from sample 24-164 (6 m) range from $-38.53 \pm 0.71\text{‰}$ to $-29.73 \pm 0.71\text{‰}$ (range=8.80‰), an average value of -32.13‰ (n=11) and a median value of -30.81‰ (n=11) (Fig. 19A).

Sample 24-161 (5.25 m) sulfide $\delta^{34}\text{S}$ range from $-20.77 \pm 0.27\text{‰}$ to $-19.87 \pm 0.27\text{‰}$ (range=0.91‰), have an average value of -20.50‰ (n=6), and a median value of -20.60‰ (n=6) (Fig. 19A).

Sulfide $\delta^{34}\text{S}$ values from sample 24-154 (2.5 m) range from $-44.44 \pm 0.54\text{‰}$ to $-23.41 \pm 0.54\text{‰}$ (range=30.55‰), an average value of -32.36‰ (n=16) and a median value of -31.42‰ (n=14) (Fig. 19A).

Sulfide $\delta^{34}\text{S}$ values from sample 24-150 (0.5 m) range from $-35.20 \pm 0.22\text{‰}$ to $-32.28 \pm 0.48\text{‰}$ (range=2.93‰), an average value of -34.06‰ (n=18) and a median value of -34.31‰ (n=18) (Fig. 19A).

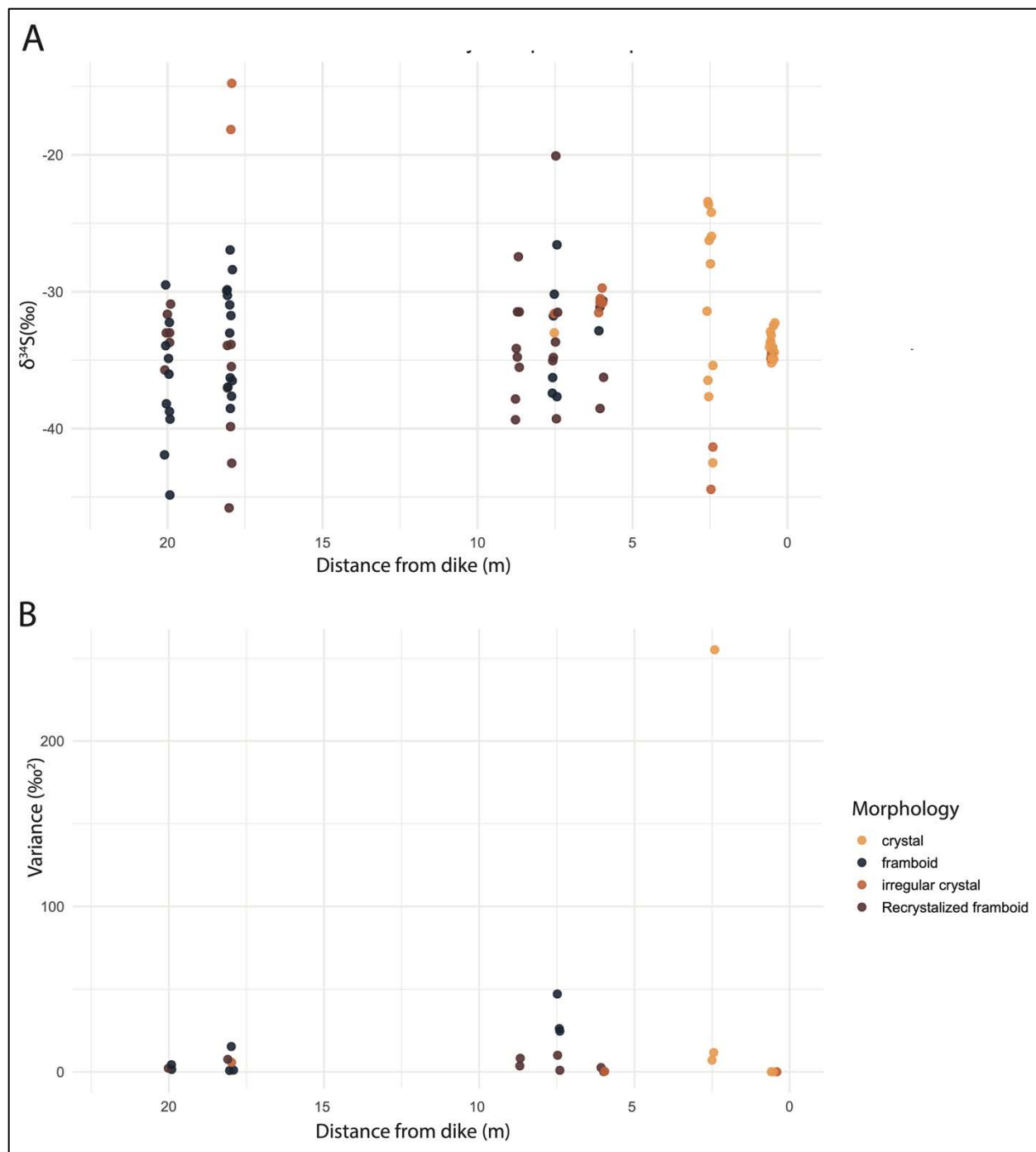


Figure 19. SIMS sulfur isotope analysis of sulfide grains. **A)** Inter-granular $\delta^{34}\text{S}$ variability of sulfide grains with distance from the dike with horizontal scatter applied to minimize

overlapping data points. **B)** Intra-granular $\delta^{34}\text{S}$ variability within sulfide grains with horizontal scatter applied to minimize overlapping data points.

B. Intra-grain $\delta^{34}\text{S}$ variability

Multiple analysis spots were placed within 26 grains. The minimum intragrain $\delta^{34}\text{S}$ range measured was 0.02‰ and the maximum was 22.59‰ (Fig. 19B). Sulfide grains from sample 24-150 (0.5 m) have intragrain ranges of 0.37‰, 0.26‰, 0.30‰, 0.02‰ (Fig. 19B). Sulfide grains from sample 24-154 (2.5 m) have intragrain ranges of -4.83‰, 3.76‰, and 22.59‰ (Fig. 19B). The sulfide grain from sample 24-161 (5.25 m) has an intragrain range of 1.09‰ (Fig. 19B). Sulfide grains from sample 24-164 (6 m) have intragrain ranges of 0.47‰, 2.28‰, and 0.77‰ (Fig. 19B). Sulfide grains from sample 24-170 (7.5 m) have intragrain ranges of 7.23‰, 9.70‰, 1.37‰, 7.02‰, and 4.48‰ (Fig. 19B). Sulfide grains from sample 24-175 (8.75 m) have intragrain ranges of 2.68‰ and 4.05‰ (Fig. 19B). Sulfide grains from sample 24-191 (18 m) have intragrain ranges of 1.28‰, 3.37‰, 5.50‰, and 5.53‰ (Fig. 19B). Sulfide grains from sample 24-193 (20 m) have intragrain ranges of 1.70‰, 2.09‰, and 2.93‰ (Fig. 19B).

Discussion

The motivation of this work is to evaluate how sulfide $\delta^{34}\text{S}$ is preserved under post-depositional thermal alteration. In this section, I first constrain the metamorphic gradient throughout the outcrop, followed by an assessment of how sulfide grains change along that gradient. Finally, I scrutinize the in-situ sulfide $\delta^{34}\text{S}$ data for quality and interpret the resulting trends within the framework of previous work outlined in the introduction.

I. Characterization of the Pierre Shale

Interpreting the sulfide $\delta^{34}\text{S}$ data requires a clear understanding of both the host rock and grains in which these measurements were made. Below, I examine organic carbon contents, bulk mineralogy, and sulfide mineralogy to establish the characteristics of the Pierre Shale and the metamorphic gradient imposed by the igneous intrusion.

A. Post-depositional thermal alteration

Total organic carbon contents and clay mineral geothermometry are used to characterize the metamorphic gradient and divide the outcrop into three zones based on the extent of heating: the Distal Zone (average TOC: 1.50 wt% , $T < 160^\circ\text{C}$), Transition Zone (average TOC: 0.89 wt%, $160^\circ\text{C} < T < 300^\circ\text{C}$), and Proximal Zone (average TOC: 0.89 wt%, $T \geq 300^\circ\text{C}$) (Fig. 20). This framework is described in the subsections below.

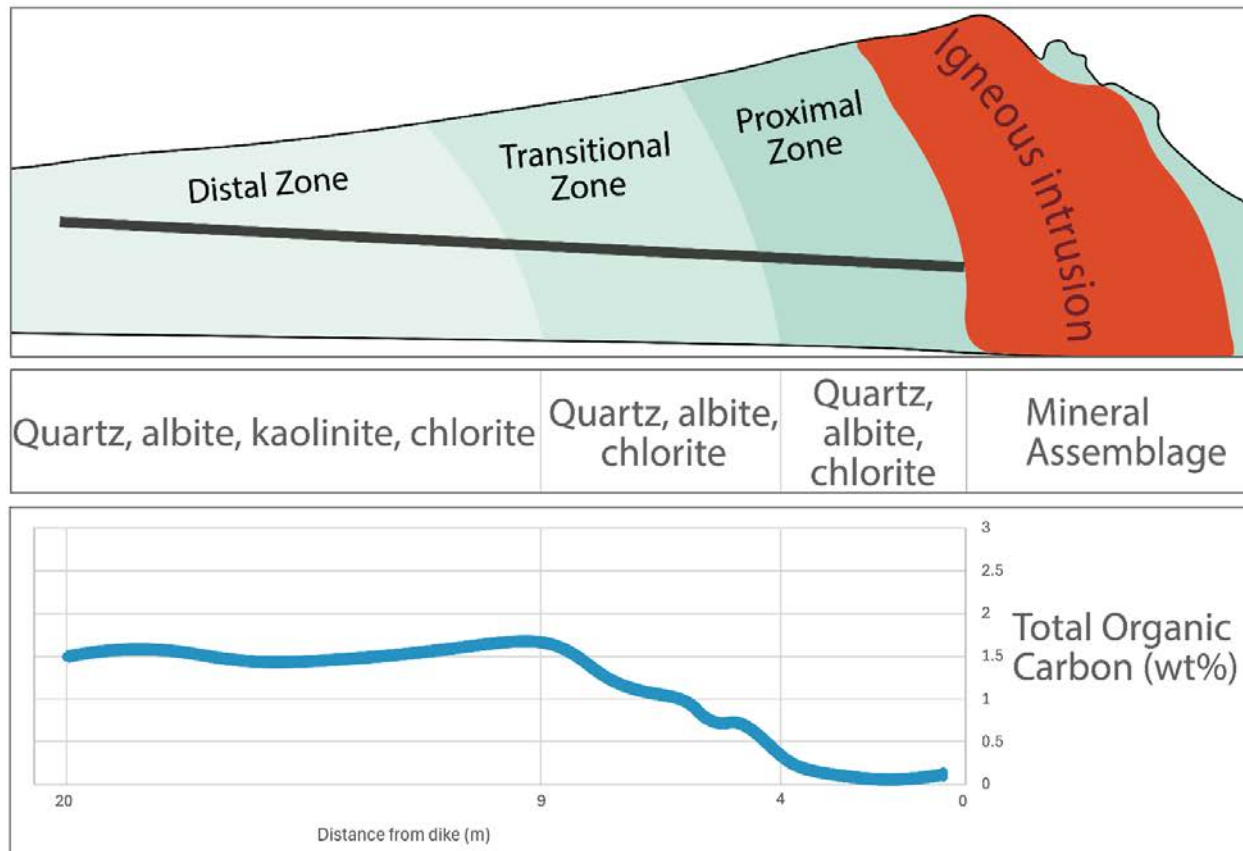


Figure 20. Total organic carbon (TOC) values and mineral assemblage dividing the Pierre Shale outcrop into three zones. Dark grey line represents sampling transect.

i. Total organic carbon geothermometry

Total organic carbon (TOC) content can be used as a proxy for thermal maturity in sedimentary rocks, reflecting the progressive decomposition of organic matter under increasing thermal stress, including that imposed by contact metamorphism (Jarvie, 1991; Aarnes et al., 2015) (Fig. 7, 20). Below, I interpret TOC trends across the outcrop to assess the extent of thermal alteration within the Pierre Shale.

TOC values decrease towards the igneous intrusion (Fig. 7, 20), indicating a potential thermal alteration gradient that peaks in the sedimentary rocks closest to the dike. The TOC trend exhibits a stepwise pattern, remaining relatively constant between 0.5 and 4.9 m from the dike, rising sharply from 4.9 to 9 m, and stabilizing again between 9 and 22 m (Fig. 7, 20).

Heating associated with contact metamorphism leads to a reduction in TOC (Aarnes et al., 2015; Mark et al., 2024), making it a good indicator of the magnitude of thermal alteration. This pattern provided a basis for subdividing the outcrop into three zones of thermal alteration: Proximal (0-5 m), Transition (5-9 m), and Distal (9-22 m). The average TOC from samples collected in the Distal, Transition, and Proximal Zones are 1.50 wt%, 0.89 wt%, and 0.11 wt%, respectively (Fig. 7, 20). These data indicate that there are three distinct zones of increasing metamorphic gradient towards the igneous intrusion (Fig. 20).

ii. Clay mineral geothermometry

Clay minerals, particularly chlorite and illite, are sensitive to hydrothermal conditions and can be used as a geothermometer in low-temperature regimes (temperature < 350°C) (Fulignati, 2020; Pereira et al., 2024).

Hydrothermal alteration occurs when fluids chemically react with existing mineral phases in the host rock, which then form new mineral assemblages that are stable in the new environment (Fulignati, 2020). By examining the mineral assemblages present in each zone of this outcrop, broad temperature constraints can be determined. Clay minerals used in this analysis are chlorite, illite, and kaolinite. Chlorite and illite are commonly stable between 160-300°C and 200-300°C, respectively, but both minerals can be present between 100-350°C (Fulignati, 2020; Pereira et

al., 2024). Kaolinite is commonly stable at temperatures between 80-160°C, but can be present at temperatures up to 220°C (Fulignati, 2020; Pereira et al., 2024).

Evidence for hydrothermal conditions associated with this intrusion comes from the presence of hornblende in the dike, which indicates that the dike was rich in magmatic water—water that likely mixed with fluids generated by the breakdown of water-rich clays within the intruded shale (Scott et al., 1990). Major element analyses of the Eagle Rock Dike further suggest that its magmatic fluids were silica- and potassium-poor (Scott et al., 1990). Such a composition would favor reactions with clay minerals, which would be more prone to alteration as the fluid–rock system sought chemical equilibrium.

The Distal Zone has the following mineral assemblage, as determined by sample 24-191 (18 m): quartz (30.01%), albite (28.36%), illite (33.74%), kaolinite (7.53%), and chlorite (0.37%). The Distal Zone composition serves as an approximation of the starting, unaltered, mineral assemblage. The presence of kaolinite in this zone indicates that temperatures did not surpass 160°C. The Transition Zone, represented by sample 24-164 (6 m), has a mineral assemblage of albite (72.20%), quartz (17.64%), and chlorite (10.15%). The loss of kaolinite indicates that temperatures reached at least 160°C, while the presence of chlorite suggests that heating likely did not exceed 300°C in this zone. The Proximal Zone has the following mineral assemblage, provided by sample 24-150 (0.5 m): quartz (69.17%), albite (30.34%), and chlorite (0.5%). The absence of kaolinite again constrains the minimum temperature to 160°C, while the continued decline in chlorite relative abundance from the Transition Zone to the Proximal Zone potentially supports increasing temperatures approaching chlorite's upper stability limit of approximately 300°C.

It should be noted that these heating constraints are limited, as only three samples were analyzed using XRD. As a result, evidence of heterogeneous heating within metamorphic regimes—which has been observed in previous studies (Baumgartner and Valley, 2001; Yallup et al., 2013)—may be missing. This topic is discussed further in Section III.A. *Heterogeneity of Metamorphic Fluid Flow*. Despite these data limitations, the combined clay mineral geothermometry and TOC thermal maturity constraints support a metamorphic gradient that increases toward the igneous intrusion at this study site. In summary, the temperature constraints of the Distal, Transition, and Proximal Zone are as follows: $< 160^{\circ}\text{C}$, $160\text{-}300^{\circ}\text{C}$, and $\geq 300^{\circ}\text{C}$.

B. Sulfide grain characterization

As thermal alteration increases from the Distal to the Proximal Zone, sulfide grains shift from framboid to crystal morphology. The effect of post-depositional heating on the sulfide minerals was investigated with scanning electron microscopy (SEM) imaging, providing insight into the metamorphic processes affecting sulfide grains.

In the Distal Zone, framboid and recrystallized framboid morphology dominate (99%), as well as $< 14\ \mu\text{m}$ grain diameters (95%). Clay mineral and TOC geothermometry indicate that this zone reflects unaltered sediments ($T < 160^{\circ}\text{C}$), therefore these patterns in sulfide morphology and size are interpreted as original sedimentary signatures.

Sulfide grains found in the Transition Zone ($160^{\circ}\text{C} < T < 300^{\circ}\text{C}$) display evidence of extensive framboid recrystallization. In this zone, framboid and recrystallized framboid morphology dominate (70%), though there is a significant portion of sulfide grains that are crystals and irregular crystals (~30%). Additionally, while grain diameters less than $14\ \mu\text{m}$ dominate (82%),

there is a significant proportion of grains displaying 15-54 μm diameters (18%). Importantly, sample 24-161 (5.25 m) preserves massive sulfide crystals (1000-2000 μm) that are not found in other samples within the Transition Zone. Additionally, sulfide grains from samples 24-175 and 24-164 display Fe-oxide rims and significant replacement by Fe-oxide minerals—a characteristic trait not found in grains of the Proximal and Distal Zones (Fig. 14, 16).

In the Proximal Zone ($T \geq 300^\circ\text{C}$), the majority of sulfide grains display crystal morphology (95%), and nearly all have diameters $<14 \mu\text{m}$ (99%). This predominance of crystalline sulfide grains is consistent with the inferred extent of thermal alteration in this zone (Åström, 2014; George et al., 2018).

Overall, framboids dominate in the Distal Zone, crystal morphologies dominate in the Proximal Zone, and the Transitional Zone exhibits the greatest variability in sulfide morphology. Both the Proximal and Distal Zones are dominated by small ($<14 \mu\text{m}$) grain sizes, whereas the Transitional Zone contains a greater proportion of larger grains ($>14 \mu\text{m}$). These observations are consistent with the transition of sulfide grains from framboid to crystal morphology expected during thermal or hydrothermal alteration (Åström, 2014; George et al., 2018).

Additionally, SEM imaging displays a decrease in pore space and clay minerals present in the matrices in Proximal Zone samples, which indicates a lower extent of recrystallization in the Transition and Distal Zones. Paring sulfide characterizations by zone with thermal constraints, I observe the replacement of framboids and subsequent precipitation of crystal sulfides with increasing thermal alteration. Further, observations from the Transition Zone also show an

increasing relative proportion of larger ($>14\ \mu\text{m}$) grain sizes occurring as sulfide grains transition from a framboid to crystal morphology.

II. In situ sulfur isotope analysis

In this work, I seek to establish how sedimentary sulfur records respond to post-depositional thermal alteration. To accomplish this, the sulfur isotope composition was measured and analyzed on the microscale using SIMS. This method allowed me to compare the $\delta^{34}\text{S}$ values both between and within sulfide grains across the thermal gradient established in the previous section. In this section, I examine trends in sulfide $\delta^{34}\text{S}$ across the metamorphic gradient and evaluate the quality of the data.

A. Sulfide $\delta^{34}\text{S}$

In this section, I use SIMS to investigate how post-depositional heating alters sulfide $\delta^{34}\text{S}$ and what this reveals about the processes controlling the preservation of sedimentary sulfide records.

The original average sulfur values defined by the Distal Zone ($T < 160^\circ\text{C}$; average: -34.10‰) are conserved in the averages of both the Transition ($150^\circ\text{C} < T < 300^\circ\text{C}$; average: -32.86‰) and Proximal ($T \geq 300^\circ\text{C}$; average: -33.35‰) Zones. The original $\delta^{34}\text{S}$ spread, however, is not conserved, narrowing from 29.50‰ (20 m) to 2.93‰ (0.5 m).

Under standard post-SIMS screening processes, the average SIMS sulfide $\delta^{34}\text{S}$ values of the Distal, Transition, and Proximal Zones are -34.10‰ , -32.86‰ , and -33.35‰ ; median sulfide $\delta^{34}\text{S}$ values of the Distal, Transition, and Proximal Zones are -33.93‰ , -31.76‰ , and -34.21‰ . Sample 24-161 (5.25 m) has been excluded from these averages due to the lack of other crystal

sizes to analyze apart from the two massive crystal sizes (1000-2000 μm) and because a single crystal was analyzed.

The Distal, Transition, and Proximal Zones samples display $\delta^{34}\text{S}$ spreads of 31.02‰, -19.28‰, and 21.03‰, respectively (Fig. 19). The spread of sulfide $\delta^{34}\text{S}$ values collected from the Proximal Zone exhibit a unique pattern. Sample 24-154 (2.5 m) exhibits a 21.03‰ spread in sulfide $\delta^{34}\text{S}$ values. The spread of sulfide $\delta^{34}\text{S}$ values sharply converges to 2.93‰ in sample 24-150 (0.5 m). Notably, while the spread of $\delta^{34}\text{S}$ values changes considerably, the average $\delta^{34}\text{S}$ across the Distal, Transition, and Proximal Zones remains stable, varying by only 1.2‰ (Fig. 19).

As thermal alteration increases, the original depositional $\delta^{34}\text{S}$ values recorded in the Distal Zone average sulfide $\delta^{34}\text{S}$ ($T < 160^\circ\text{C}$; average: -34.10‰) are broadly conserved in the average sulfide $\delta^{34}\text{S}$ in the Transition Zone ($200^\circ\text{C} < T < 300^\circ\text{C}$; average: -32.86‰) and the Proximal Zone ($T \geq 300^\circ\text{C}$; average: -33.35‰) (Fig. 19).

These trends in sulfur isotope data coincide with changes in sulfide morphology and size, as well as changes in post-depositional thermal alteration. Clay mineral geothermometry in the Distal Zone ($T < 160^\circ\text{C}$) indicates that the distribution in morphology, grain size, and sulfur isotope values represents original variability. Heating constraints in the Transition Zone indicate that sediments have been heated to 160-300°C, resulting in a shift from the framboid morphology, which dominates in the Distal Zone, to primarily recrystallized framboid, crystal, and irregular crystal morphologies. This shift coincides with larger sulfide grain sizes in the Transition Zone.

Based on the above constraints on post-depositional thermal alteration, I find that original depositional trends in average $\delta^{34}\text{S}$ composition are conserved under heating up to at least 300°C , though the depositional variability of $\delta^{34}\text{S}$ is not conserved throughout the metamorphic gradient (Fig. 19).

B. Pyrite and pyrrhotite $\delta^{34}\text{S}$

An important step in SIMS analysis is evaluating data quality. Although the analyses discussed in the previous section passed standard post-SIMS screening, elevated relative yield values prompted a more detailed investigation. This investigation revealed that many high-yield grains were pyrrhotite rather than pyrite, requiring a reassessment of the sulfide $\delta^{34}\text{S}$ trends previously discussed.

Upon further examination, some analyzed spots had relative yield values higher than typically expected for SIMS measurements. Despite this, these data displayed typical trends in $^{32}\text{SH}/^{32}\text{S}$ ratios, standard errors, and pit morphology, and were therefore retained during the standard post SIMS screening process (Fig. 21).

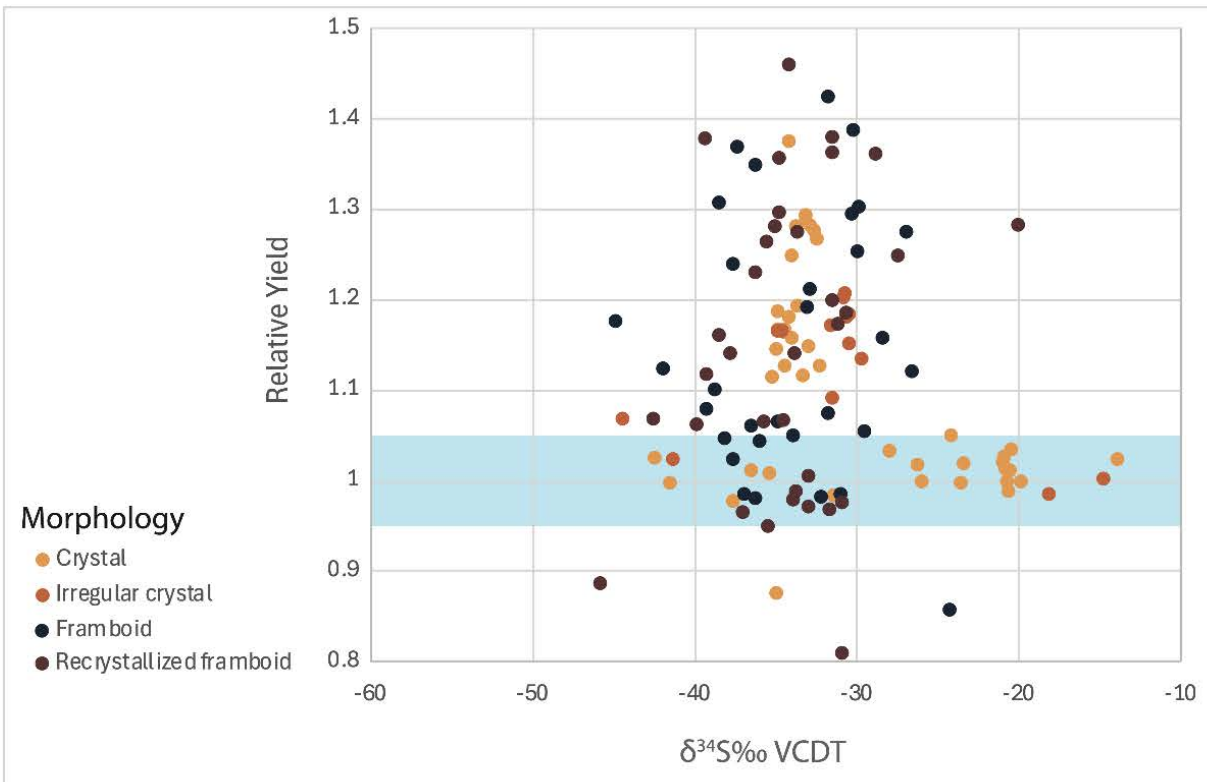


Figure 21. Relative yield trends with respect to sulfide $\delta^{34}\text{S}$ and morphology, acceptable relative yield value range 0.95-1.05 highlighted in blue.

Acceptable relative yields for SIMS analyses typically lie between 0.95 and 1.05 (Fig. 21).

Many of the sulfide analyses lie above this range (Fig. 21) so to ensure that average $\delta^{34}\text{S}$ trends were not biased by these erroneous data, analyses outside this range were removed and the remaining data were evaluated relative to distance from the dike (Fig. 22). This process will be referred to as advanced post-SIMS screening. Despite screening out 71 analyses, trends in grain $\delta^{34}\text{S}$ with distance indicate that, even in this refined dataset, sample-averaged sulfide $\delta^{34}\text{S}$ values do not change significantly during contact metamorphism up to at least 300°C (Figs. 19, 22).

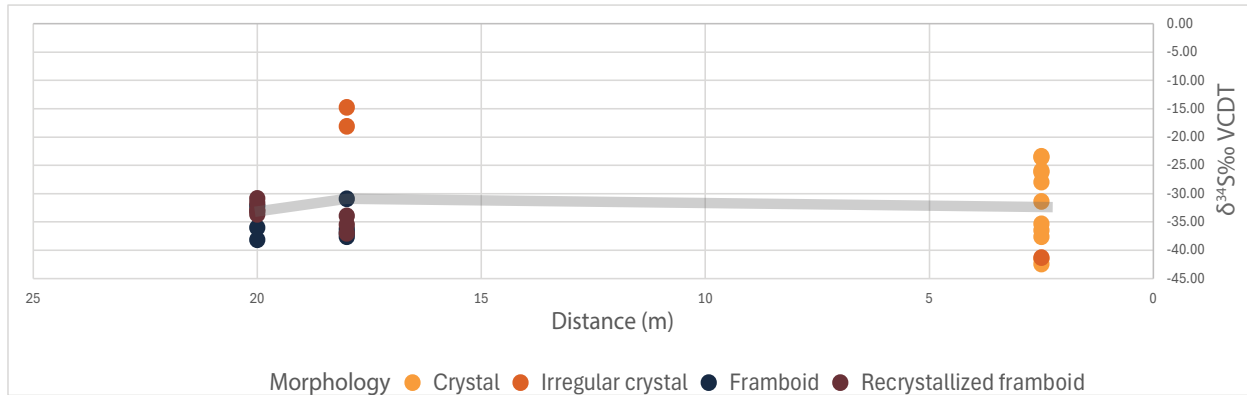


Figure 22. Grain $\delta^{34}\text{S}$ values that displayed a relative yield between 0.95 and 1.05 during SIMS analysis with respect to distance from dike. Average values within a sample labeled and indicated with a horizontal gray line.

III. Effects of hydrothermal fluids on sedimentary sulfur records.

Previous sections characterized the metamorphic gradient associated with the intrusion and detailed its influence on sulfide mineralogy, morphology, and sulfur isotope compositions. However, further investigation is needed to better understand how hydrothermal fluids interacted with the Pierre Shale. In this section, I evaluate how hydrothermal fluid flow and desulfurization processes contributed to the observed sulfide $\delta^{34}\text{S}$ trends and mineralogical changes, integrating these findings with prior work on these topics.

A. Heterogeneity of metamorphic fluid flow

In this section, I investigate the irregular distribution of pyrite and pyrrhotite across the metamorphic gradient. I place these observations in the context of existing work on magmatic fluid flow and fluid–rock interactions. Silicate dehydration and water-rich mafic intrusion established hydrothermal conditions within the Pierre Shale, driving heterogeneous fluid flow that produced spatially variable sulfide alteration. Along these pathways, circulating fluids

reacted with pyrite to form pyrrhotite, while increases in bulk sulfur toward the dike may suggest sulfur addition from magmatic fluids.

Although the extent of interaction between sulfides and fluids remains uncertain, the presence of sulfur-rich fluids may have limited sulfur exchange between the fluid and pyrite. While heating facilitated the recrystallization of pyrite from framboids to crystals, sulfur rich fluids may have played a role in preserving original average pyrite $\delta^{34}\text{S}$ across zones of increasing metamorphism. Some aspect of the system must have operated to buffer exchange of sulfur isotopes and loss from the system.

Standard post-SIMS screening flagged analyses with high relative yields, which may suggest analysis of pyrrhotite (FeS) rather than pyrite (FeS_2). Notably, pyrrhotite can be difficult to distinguish from pyrite with SEM imaging alone, therefore may not have been identified during the pre-SIMS imaging process. A representative subset of grains was analyzed for sulfide mineralogy using EDS analysis (Fig. 23, 24). This subset included a range of $\delta^{34}\text{S}$ values, relative yields, and grain morphologies (Fig. 23, 24). These results show that sulfide mineralogy (i.e. pyrite or pyrrhotite) largely accounts for elevated relative yields in samples collected 0.5, 6, 7.5, 8.75, and 18 m (samples 24-150, 24-164, 24-170, 24-175, and 24-191, respectively) from the igneous intrusion (Fig. 23, 24).

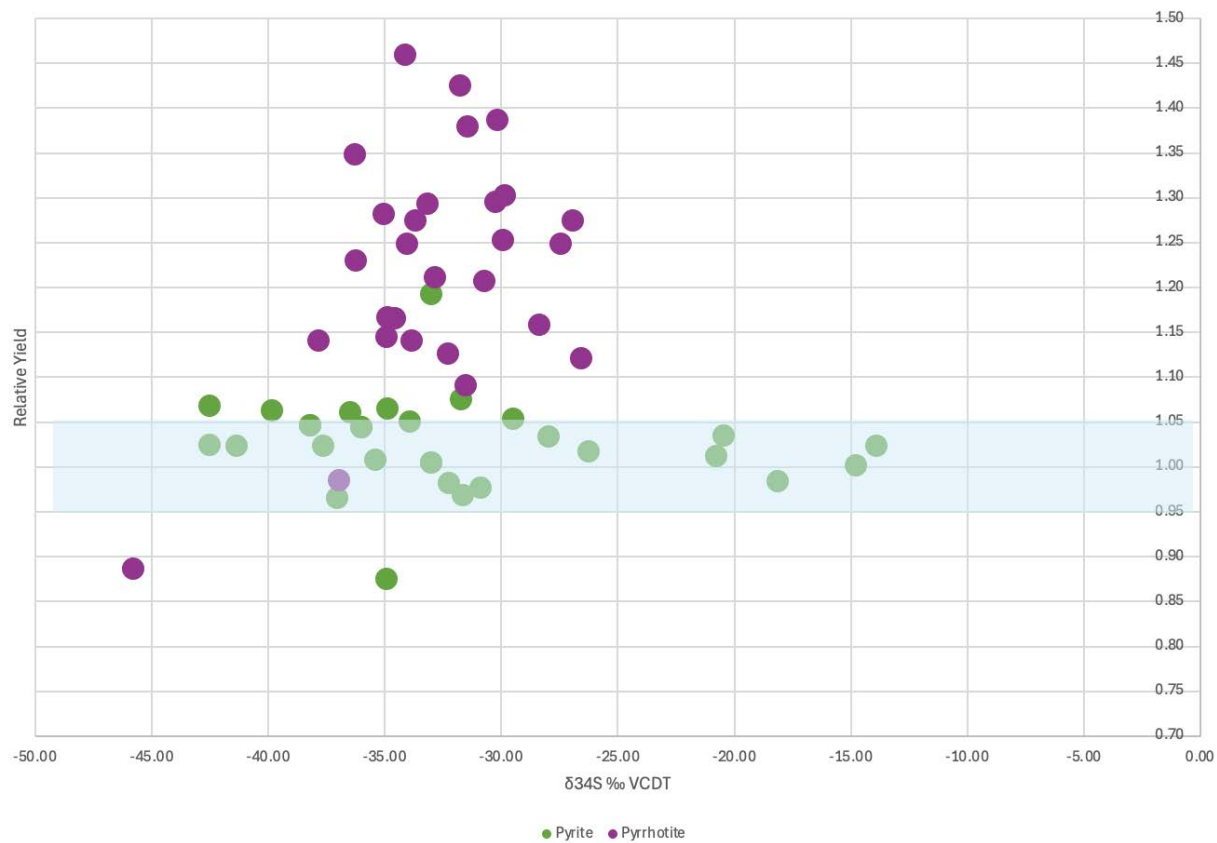


Figure 23. Relative yield trends with respect to grain $\delta^{34}\text{S}$ and mineralogy, acceptable relative yield value range 0.95-1.05 highlighted in blue.

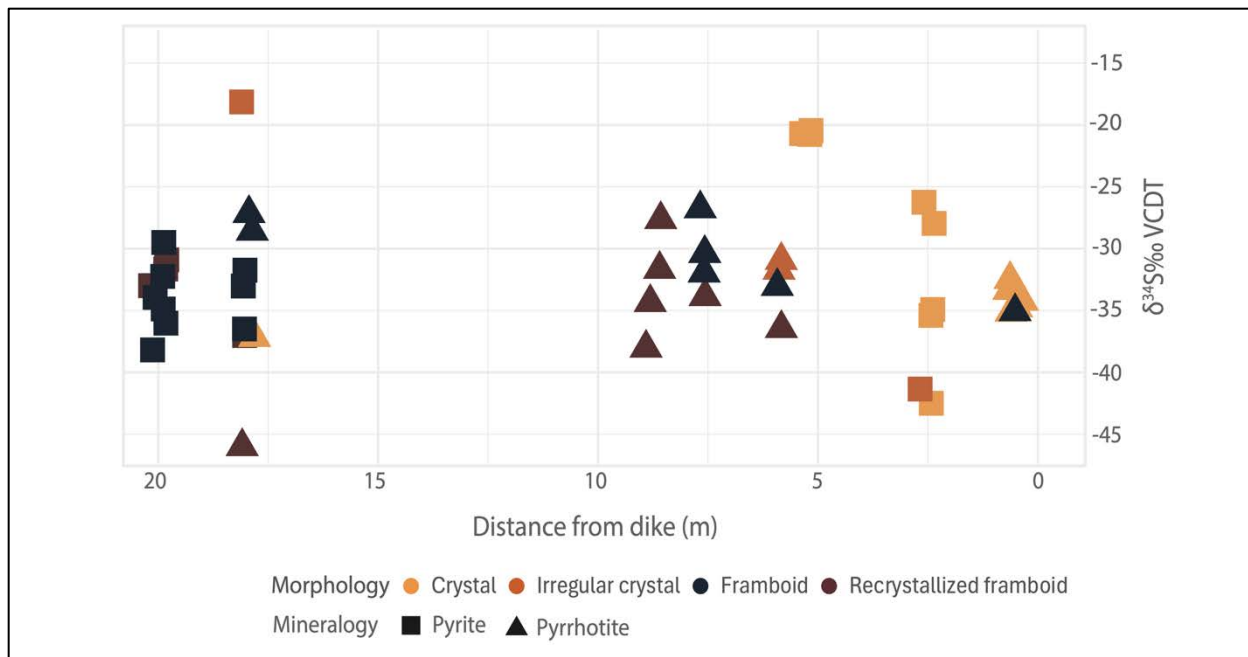


Figure 24. Spatial distribution of grain mineralogy determined by EDS analysis on a subset of sulfide grains analyzed for $\delta^{34}\text{S}$.

The results of EDS analysis show that grains with relative yields up to 1.1 have Fe:S ratios consistent with pyrite. To accommodate this effect, the acceptable relative yield range established during advanced post-SIMS screening was expanded from 0.95–1.05 to 0.95–1.10. The $\delta^{34}\text{S}$ analyses that produced relative yields within this range were evaluated with respect to distance from the dike. While expanding the acceptable relative yield range does not affect the trends in sample-averaged $\delta^{34}\text{S}$ pyrite values, this dataset offers limited resolution on how Transition Zone $\delta^{34}\text{S}$ pyrite values fit into these trends (Fig. 25). The addition of a single analysis in the Transition Zone closely matches the average $\delta^{34}\text{S}$ pyrite values in the Distal and Proximal Zone (Fig. 25).

These data also show spatial variability of sulfide minerals, rather than following a linear trend (Fig. 24). EDS analysis shows that samples collected from 20, 5.25, and 2.5 m (samples 24-193, 24-161, and 24-154, respectively) from the intrusion contain only pyrite minerals, while samples collected from 8.75, 7.5, 6, and 0.5 m (samples 24-175, 24-170, 24-164, and 24-150, respectively) from the intrusion contain only pyrrhotite (Fig. 24). Only sample 24-191 (18 m) contains both pyrite and pyrrhotite (Fig. 24).

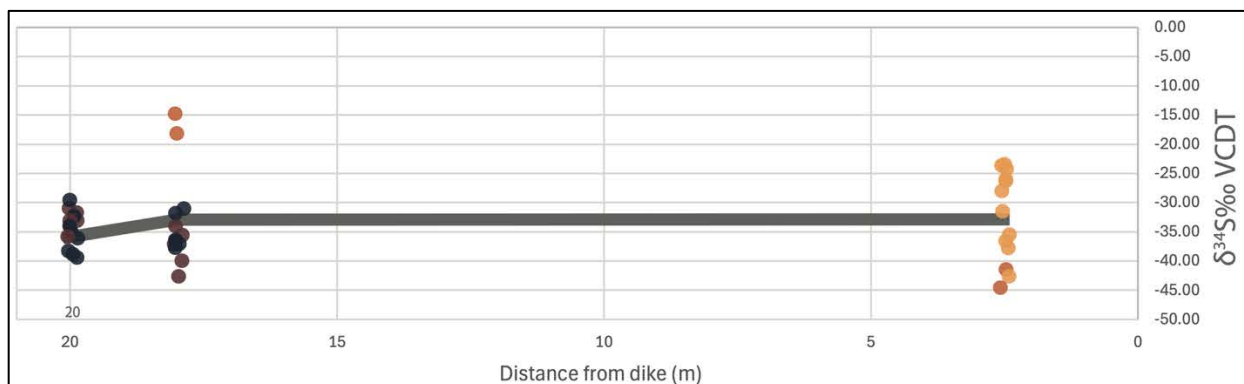


Figure 25. Pyrite grain $\delta^{34}\text{S}$ values that displayed a relative yield between 0.95 and 1.10 during SIMS analysis with respect to distance from dike. Average values within a sample labeled and indicated with a horizontal gray line.

One explanation for the irregular spatial distribution of pyrite and pyrrhotite is desulfurization of the shale due to interaction with sulfur-poor hydrothermal fluids. Desulfurization is a process in which sulfur is removed from sediments during contact metamorphism (Tomkins, 2010; Yallup et al., 2013). The dehydration of silicates under metamorphic conditions produces fluids, which leads to the liberation of sulfur from pyrite to maintain equilibrium between minerals and the sulfur-poor fluids (buffering effect) (Tomkins, 2010). The breakdown of pyrite (FeS_2) to pyrrhotite (FeS) produces this sulfur (Eqn. 5) (Tomkins, 2010).



Equation 5. Breakdown of pyrite to pyrrhotite.

Multiple generations of magma and heterogeneous fluid flow may account for the irregular pattern of pyrrhotite formation with respect to distance from the intrusion (Fig. 24). It has been suggested that the Eagle Rock Dike is compound, or made up of successive injections of magma (Scott et al., 1990), which can produce complex alteration patterns in host rocks (Aarnes et al., 2011; Pattison and Forshaw, 2025). Heterogeneous fluid flow may also contribute to this irregular pattern in sulfide mineralogy.

Fluid migration through sediments during contact metamorphism is not always homogenous, as fluid flow can be constrained to high permeability zones such as grain boundaries, cracks, vein systems, or more permeable lithology (Baumgartner and Valley, 2001). Mineral veins seen in the Proximal and Transition Zones may provide evidence for channelized fluid flow (Fig. 26).

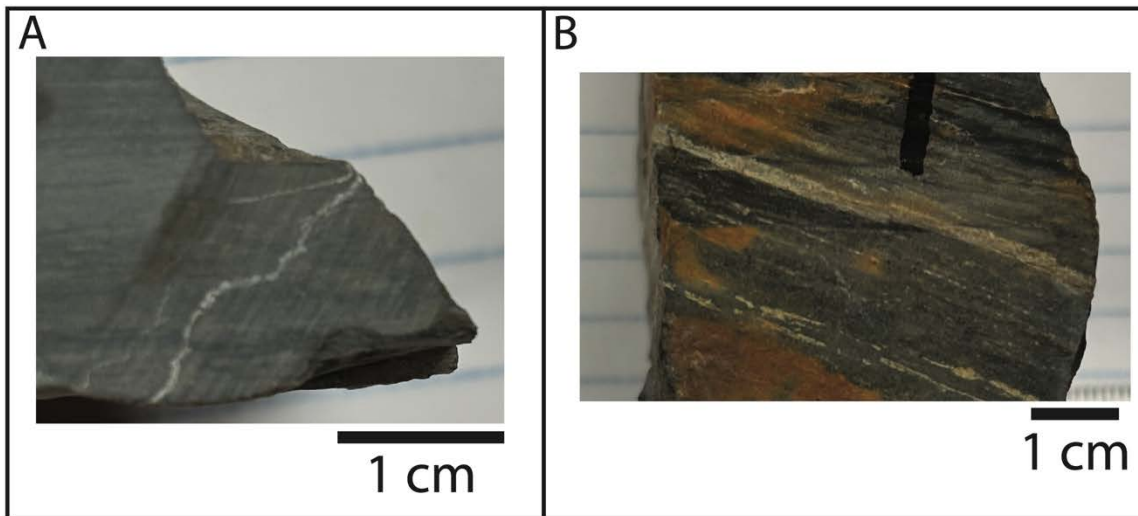


Figure 26. Mineral veins in whole rock samples **A)** 24-161 (5.25 m) and **B)** 24-154 (2.5 m).

This type of fluid flow can lead to heterogeneity in hydrothermal alteration, allowing some rock to become more extensively infiltrated and thus altered relative to others (Baumgartner and Valley, 2001). While TOC analysis and clay mineral geothermometry presents a metamorphic gradient that increases towards the igneous intrusion, these EDS mineralogy data suggest a more spatially complex alteration (Fig. 24).

B. Sulfur exchange with metamorphic fluids

While the breakdown of pyrite to pyrrhotite may suggest the presence of sulfur-poor fluids generated by silicate dehydration, an increase in bulk sulfur towards the intrusion may indicate an additional sulfur-rich fluid source. The presence of hornblende in the Eagle Rock Dike suggests that the intrusion may have contributed magmatic water to the hydrothermal fluids in this setting (Scott et al., 1990). Magmatic water could have caused sulfur migration or introduced sulfur-bearing fluids to the sediments, leading to an increase in bulk sulfur (Haughton et al., 1974; Wallace and Carmichael, 1992). This increase occurred, not in the Fe-sulfide fraction, but in the Ca-sulfate fraction.

Total sulfur contents were measured in bulk and acid treated sample fractions to further investigate the effect of hydrothermal alteration on the sulfur phases within sediments. Total sulfur contents from the bulk rock fraction increase from the Distal to the Proximal Zone, averaging 0.58 wt% in the Distal Zone, 0.80 wt% in the Transition Zone, and 1.10 wt% in the Proximal Zone (Fig. 28). The bulk fraction can represent the following sources of sulfur: organic sulfur, Fe-sulfides (e.g. pyrite, pyrrhotite, elemental sulfur, barite, and carbonate-associated sulfate and Ca-sulfate (e.g. Anhydrite or gypsum). Elemental sulfur, barite, and carbonate associated sulfate are not likely major contributors to this increase in sulfur because elemental

sulfur is highly reactive, barite would have been noted in XRD analysis, and bulk carbon contents decreases towards the intrusion (Fig. 7). This indicates that organic sulfur, Fe-sulfides, and Ca-sulfate are potential contributors to this increase in bulk sulfur.

Constraining which sources of sulfur contribute to this increase in total sulfur contents can be achieved by comparing bulk total sulfur contents with decarbonated total sulfur contents. Below, trends in the decarbonated fraction will be evaluated and compared to the bulk fraction.

The decarbonated fraction can represent the following potential sources of sulfur: organic sulfur, Fe-sulfide, and barite, though barite is not a likely contributor as it would have been noted in XRD analysis. The decarbonation process will remove carbonate-associated sulfate, Ca-sulfate, and can remove iron sulfide species if left in strong acid too long—though this is unlikely considering the dilute acid used in the decarbonation process and no evidence of systematic change across samples that were treated similarly. Acid insoluble sulfur contents for the Distal, Transition, and Proximal Zone average 0.39, 0.37, and 0.40 wt%, respectively (Fig. 27). The average contents for each zone do not change significantly, though it should be noted that there is greater variability in the Transition and Proximal Zones (Fig. 27) Overall, the trend in sulfur contents for this fraction varies a negligible .03 wt% suggesting the organic sulfur and Fe-sulfide contents are relatively stable throughout the increasing Distal, Transition, and Proximal Zones. When considered alongside the increase in acid soluble content toward the intrusion, these data suggest that the elevated sulfur may reflect an addition of Ca-sulfate (e.g. Anhydrite or gypsum) in the Transition and Proximal Zones (Fig. 27).

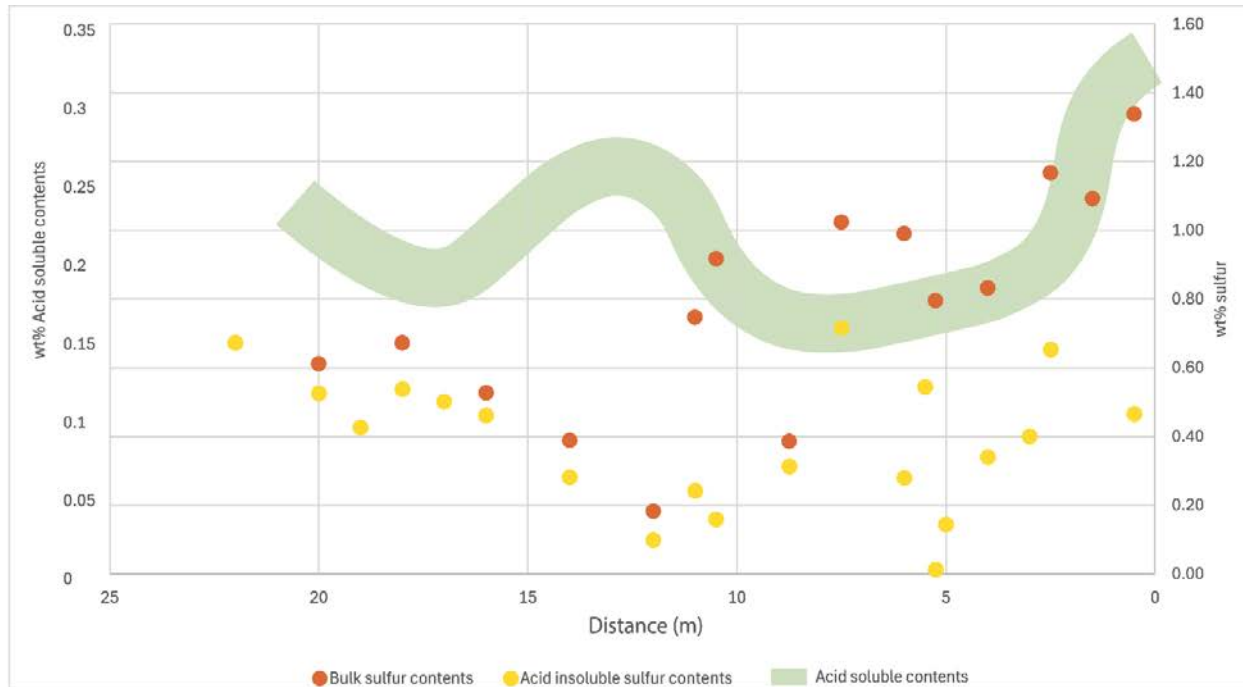


Figure 27. Trends in bulk sulfur contents, acid insoluble sulfur contents, and acid soluble contents with respect to distance from dike.

These results are contrary to the principles of desulfurization, which is the process of sulfur removal from sediments during contact metamorphism through the breakdown of pyrite (FeS_2) to pyrrhotite (Eqn. 5) (Tomkins, 2010; Yallup et al., 2013). While the presence of pyrrhotite provides evidence that desulfurization occurred in these sediments, the sulfide content, represented in the acid insoluble sulfur contents, does not indicate significant loss of sulfur across the metamorphic gradient (Fig. 27).

Desulfurization is often accompanied by the isotopic fractionation of sulfur in which the lighter isotope of sulfur (^{32}S) is preferentially mobilized (Amrani et al., 2005; Yallup et al., 2013). The remaining sulfide, pyrrhotite, is left more depleted in ^{32}S relative to the H_2S gas product (Yallup

et al., 2013). However, pyrrhotite $\delta^{34}\text{S}$ is not able to be properly analyzed in this study as a pyrrhotite standard was not measured during SIMS analyses.

Yamamoto (1984) offers a different perspective on the desulfurization process through a laboratory experiment investigating sulfur isotope effects during the thermal breakdown of pyrite. The study tracked the evolution of pyrite $\delta^{34}\text{S}$ values during incremental heating and found that these values remained nearly identical to those of the initial pyrite until approximately 80% of the reaction was complete, after which the residual pyrite became appreciably enriched in ^{34}S (Yamamoto, 1984). This perspective may provide a basis for the observed consistency in pyrite $\delta^{34}\text{S}$ values across the metamorphic gradient in this outcrop (Fig. 25).

When considering the stability of average pyrite $\delta^{34}\text{S}$ across the thermal gradient, additional consideration should go to sulfur-rich magmatic fluids. If a sulfur exchange occurred between the magmatic fluids and the sulfide minerals within the Pierre Shale, a shift in pyrite $\delta^{34}\text{S}$ values towards mantle sulfur values ($\sim 0\text{‰}$) would be expected (Fig. 2) (Bottrell and Newton, 2006). However, the pyrite $\delta^{34}\text{S}$ data do not exhibit a shift toward mantle values and therefore do not support extensive sulfur exchange between pyrite and magmatic fluids in this setting (Fig. 25).

One possible explanation for this trend is that sulfur exchange may have been limited due to the sulfur-rich nature of both the fluids and the pyrite, potentially contributing to the preservation of original pyrite $\delta^{34}\text{S}$ (Fig. 25). Understanding why original sedimentary sulfur isotope values appear to persist in this setting—despite interaction with sulfur-rich magmatic fluids and pyrite recrystallization—requires further investigation.

Conclusions

I find that the depositional sedimentary sulfur isotope signatures in the Pierre Shale are conserved across zones of increasing metamorphism up to $\sim 300^{\circ}\text{C}$. Sulfur-rich magmatic fluids and relatively low temperatures of alteration may have enhanced the retention of original average pyrite $\delta^{34}\text{S}$ values in this hydrothermal setting. Heterogeneous fluid flow produced an irregular distribution of sulfide minerals as fluids reacted with pyrite to form pyrrhotite and increases in bulk sulfur toward the dike suggest possible sulfur addition from magmatic sources and anhydrite deposition. Although heating promoted the recrystallization of pyrite from framboids to crystals, the presence of sulfur-rich fluids may have limited sulfur exchange, providing a potential mechanism for the preservation of original average pyrite $\delta^{34}\text{S}$ across the metamorphic gradient. Further investigation is needed to understand why original depositional sulfur isotope values appear to be retained in this setting despite interaction with sulfur-rich magmatic fluids and pyrite recrystallization. Given the difficulty of modeling these hydrothermal processes in laboratory experiments, continued field-based studies are critical for assessing the roles of both thermal alteration and fluid flow.

This work supports interpretations of measured $\delta^{34}\text{S}$ values of hydrothermally altered sediments as well as supports future studies on wider degrees of hydrothermal alteration and the development of correction models for reconstructing original $\delta^{34}\text{S}$. Further, these findings may allow for measuring $\delta^{34}\text{S}$ on rocks previously deemed unsuitable for analysis and interpretation.

This work contributes a field-based assessment of sulfur isotope preservation in low-grade metamorphic environments; however, questions remain concerning their stability at higher metamorphic grades ($>350^{\circ}\text{C}$) and the mechanisms responsible for the formation of pyrrhotite as far as 18 m from the intrusion.

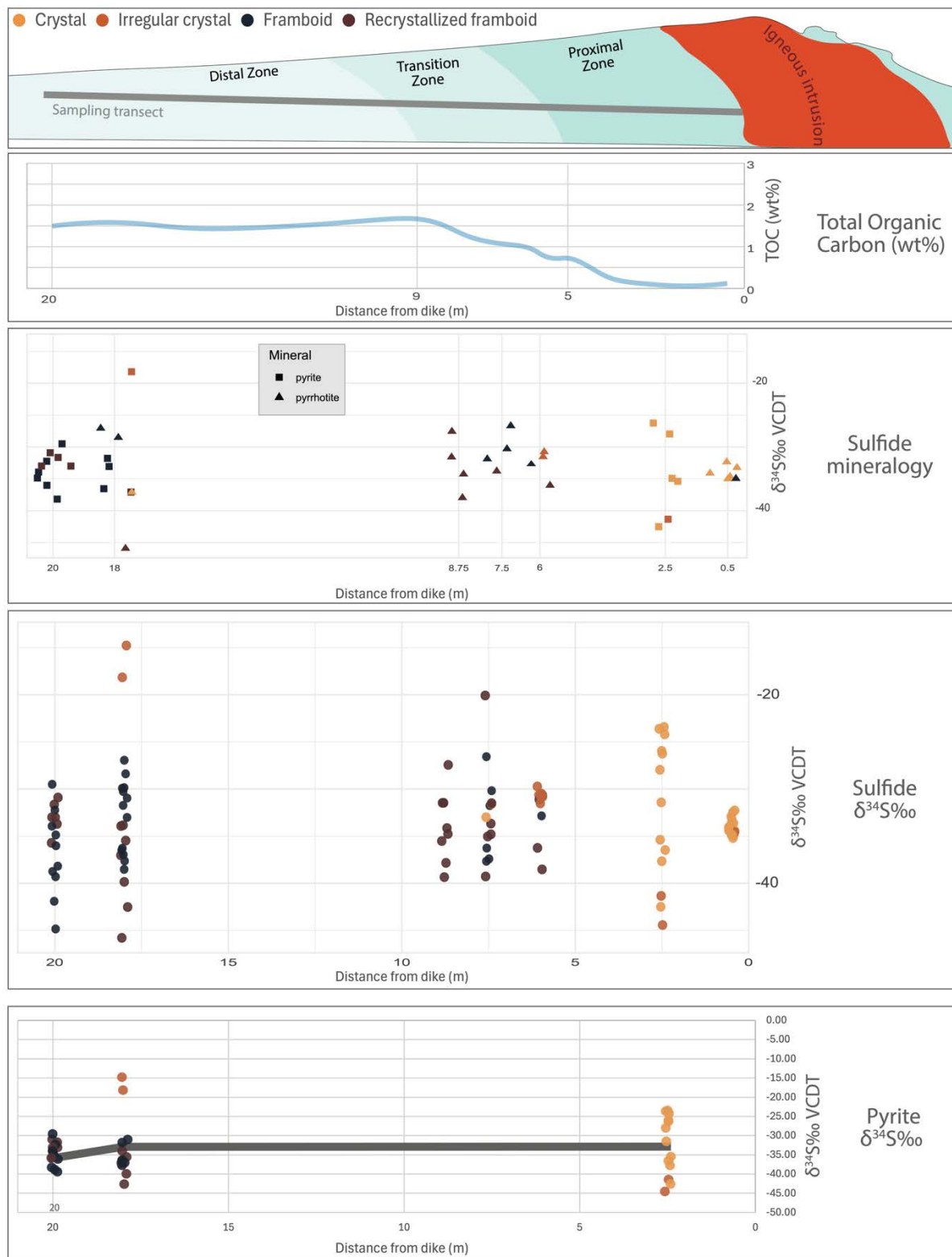


Figure 28. Conservation of sulfide and pyrite $\delta^{34}\text{S}$ across the heterogeneous metamorphic gradient in the Pierre Shale induced by the intrusion of the Eagle Rock Dike.

References

- Aarnes, I., Planke, S., Trulsvik, M., and Svensen, H., 2015, Contact metamorphism and thermogenic gas generation in the Vøring and Møre basins, offshore Norway, during the Paleocene–Eocene thermal maximum: *Journal of the Geological Society*, v. 172, p. 588–598, doi:10.1144/jgs2014-098.
- Aarnes, I., Svensen, H., Polteau, S., and Planke, S., 2011, Contact metamorphic devolatilization of shales in the Karoo Basin, South Africa, and the effects of multiple sill intrusions: *Chemical Geology*, v. 281, p. 181–194, doi:10.1016/j.chemgeo.2010.12.007.
- Amrani, A., Lewan, M.D., and Aizenshtat, Z., 2005, Stable sulfur isotope partitioning during simulated petroleum formation as determined by hydrous pyrolysis of Ghareb Limestone, Israel: *Geochimica et Cosmochimica Acta*, v. 69, p. 5317–5331, doi:10.1016/j.gca.2005.06.026.
- Amrani, A., Said-Ahamed, W., Lewan, M.D., and Aizenshtat, Z., 2006, Experiments on $\delta^{34}\text{S}$ mixing between organic and inorganic sulfur species during thermal maturation: *Geochimica et Cosmochimica Acta*, v. 70, p. 5146–5161, doi:10.1016/j.gca.2006.07.030.
- Åström, O., 2014, Sulfide mineralogy in the Ballachulish contact metamorphic Aureole: *Geochimica et Cosmochimica Acta*, v. 70, p. 5146–5161, doi:10.1016/j.gca.2006.07.030.
- Baltz, E.H., 1965, Stratigraphy and History of Raton Basin and Notes on San Luis Basin, Colorado-New Mexico: *AAPG Bulletin*, v. 49, p. 2041–2075, doi:10.1306/A6633882-16C0-11D7-8645000102C1865D.
- Baumgartner, L.P., and Valley, J., 2001, Stable Isotope Transport and Contact Metamorphic Fluid Flow: *Geochimica et Cosmochimica Acta*, v. 65, p. 1031–1044, doi:10.1016/S0016-7037(01)00103-1.
- Berner, R.A., 1984, Sedimentary pyrite formation: An update: *Geochimica et Cosmochimica Acta*, v. 48, p. 605–615, doi:10.1016/0016-7037(84)90089-9.
- Berner, R.A., and Canfield, D.E., 1989, A new model for atmospheric oxygen over Phanerozoic time: *American Journal of Science*, v. 289, p. 333–361, doi:10.2475/ajs.289.4.333.
- Berry, K., 2018, Baculites (Ammonoidea) and the age of the Pierre Shale in the eastern Raton Basin, south-central Colorado: *New Mexico Geology*, v. 40, p. 1–5, doi:10.58799/NMG-v40n1.1.
- Bottrell, S.H., and Newton, R.J., 2006, Reconstruction of changes in global sulfur cycling from marine sulfate isotopes: *Earth-Science Reviews*, v. 75, p. 59–83, doi:10.1016/j.earscirev.2005.10.004.
- Bryant, R.N., Houghton, J.L., Jones, C., Pasquier, V., Halevy, I., and Fike, D.A., 2023, Deconvolving microbial and environmental controls on marine sedimentary pyrite sulfur isotope ratios: *Science*, v. 382, p. 912–915, doi:10.1126/science.adg6103.
- Bryant, R.N., Jones, C., Raven, M.R., Owens, J.D., and Fike, D.A., 2020, Shifting modes of iron sulfidization at the onset of OAE-2 drive regional shifts in pyrite $\delta^{34}\text{S}$ records: *Chemical Geology*, v. 553, p. 119808, doi:10.1016/j.chemgeo.2020.119808.
- Bush, M.A., Horton, B.K., Murphy, M.A., and Stockli, D.F., 2016, Detrital record of initial basement exhumation along the Laramide deformation front, southern Rocky Mountains: *Geology*, v. 44, p. 1031–1034, doi:10.1130/G430001.1.

- Raton Basin Provenance Analysis: *Tectonics*, v. 35, p. 2117–2130, doi:10.1002/2016TC004194.
- Canfield, D.E., 2001, Biogeochemistry of Sulfur Isotopes: Reviews in Mineralogy and Geochemistry, v. 43, p. 607–636, doi:10.2138/gsrmg.43.1.607.
- Canfield, D.E., and Teske, A., 1996, Late Proterozoic rise in atmospheric oxygen concentration inferred from phylogenetic and sulphur-isotope studies: *Nature*, v. 382, p. 127–132, doi:10.1038/382127a0.
- Cooper, J.R., Crelling, J.C., Rimmer, S.M., and Whittington, A.G., 2007, Coal metamorphism by igneous intrusion in the Raton Basin, CO and NM: Implications for generation of volatiles: *International Journal of Coal Geology*, v. 71, p. 15–27, doi:10.1016/j.coal.2006.05.007.
- Cui, H., Kitajima, K., Spicuzza, M.J., Fournelle, J.H., Denny, A., Ishida, A., Zhang, F., and Valley, J.W., 2018, Questioning the biogenicity of Neoproterozoic superheavy pyrite by SIMS: *American Mineralogist*, v. 103, p. 1362–1400, doi:10.2138/am-2018-6489.
- Dane, C., and Bachman, G., 1962, Preliminary geologic map of the northeastern part of New Mexico | U.S. Geological Survey: <https://www.usgs.gov/maps/preliminary-geologic-map-northeastern-part-new-mexico> (accessed November 2025).
- Ding, T., Valkiers, S., Kipphardt, H., De Bièvre, P., Taylor, P.D.P., Gonfiantini, R., and Krouse, R., 2001, Calibrated sulfur isotope abundance ratios of three IAEA sulfur isotope reference materials and V-CDT with a reassessment of the atomic weight of sulfur: *Geochimica et Cosmochimica Acta*, v. 65, p. 2433–2437, doi:10.1016/S0016-7037(01)00611-1.
- Fakhræe, M. et al., 2024, The history of Earth’s sulfur cycle: *Nature Reviews Earth & Environment*, v. 6, p. 106–125, doi:10.1038/s43017-024-00615-0.
- Fang, Y., and Xu, H., 2019, A New Approach To Quantify the Ordering State of Protodolomite Using XRD, TEM, and Z-Contrast Imaging: *Journal of Sedimentary Research*, v. 89, p. 537–551, doi:10.2110/jsr.2019.29.
- Fulginiti, P., 2020, Clay Minerals in Hydrothermal Systems: *Minerals*, v. 10, p. 919, doi:10.3390/min10100919.
- Gautier, D.L., 1985, Sulfur/carbon ratios and sulfur isotope composition of some Cretaceous shales from the Western Interior of North America: U.S. Geological Survey, 85–514, doi:10.3133/ofr85514.
- George, L.L., Biagioni, C., D’Orazio, M., and Cook, N.J., 2018, Textural and trace element evolution of pyrite during greenschist facies metamorphic recrystallization in the southern Apuan Alps (Tuscany, Italy): Influence on the formation of Tl-rich sulfosalt melt: *Ore Geology Reviews*, v. 102, p. 59–105, doi:10.1016/j.oregeorev.2018.08.032.
- Halevy, I., Fike, D.A., Pasquier, V., Bryant, R.N., Wenk, C.B., Turchyn, A.V., Johnston, D.T., and Claypool, G.E., 2023, Sedimentary parameters control the sulfur isotope composition of marine pyrite: *Science*, v. 382, p. 946–951, doi:10.1126/science.adh1215.
- Harrison, A.G., and Thode, H.G., 1958, Mechanism of the bacterial reduction of sulphate from isotope fractionation studies: *Transactions of the Faraday Society*, v. 54, p. 84, doi:10.1039/tf9585400084.
- Haughton, D.R., Roeder, P.L., and Skinner, B.J., 1974, Solubility of Sulfur in Mafic Magmas: *Economic Geology*, v. 69, p. 451–467, doi:10.2113/gsecongeo.69.4.451.
- Houghton, J.L., Jones, C., and Fike, D.A., 2024, Evaluating intragrain gradients in the $\delta^{34}\text{S}$ of

- pyrite using a 7f-GEO SIMS: *Chemical Geology*, v. 668, p. 122335, doi:10.1016/j.chemgeo.2024.122335.
- Jarvie, D.M., 1991, Total Organic Carbon (TOC) Analysis, *in* Merrill, R.K. ed., *Source and migration processes and evaluation techniques*, American Association of Petroleum Geologists, p. 0, doi:10.1306/TrHbk543C11.
- Johnson, R.B., and Wood, G.H., Jr., 1956, Stratigraphy of Upper Cretaceous and Tertiary Rocks of Raton Basin, Colorado and New Mexico: *AAPG Bulletin*, v. 40, p. 707–721, doi:10.1306/5CEAE400-16BB-11D7-8645000102C1865D.
- Jones, G.E., and Starkey, R.L., 1957, Fractionation of Stable Isotopes of Sulfur by Microorganisms and Their Role in Deposition of Native Sulfur: *Applied Microbiology*, v. 5, p. 111–118, doi:10.1128/am.5.2.111-118.1957.
- Kaplan, I.R., and Rittenberg, S.C., 1964, Microbiological Fractionation of Sulphur Isotopes: *Journal of General Microbiology*, v. 34, p. 195–212, doi:10.1099/00221287-34-2-195.
- Leavitt, W., 2014, On the mechanisms of sulfur isotope fractionation during microbial sulfate reduction.
- Maynard, J.B., 1980, Sulfur isotopes of iron sulfides in Devonian-Mississippian shales of the Appalachian Basin; control by rate of sedimentation: *American Journal of Science*, v. 280, p. 772–786, doi:10.2475/ajs.280.8.772.
- Merewether, E.A., Cobban, W.A., and Obradovich, J.D., 2011, Biostratigraphic data from Upper Cretaceous formations-eastern Wyoming, central Colorado, and northeastern New Mexico: *U.S. Geological Survey 3175*, doi:10.3133/sim3175.
- Owens, J.D., 2019, Application of Thallium Isotopes: Tracking Marine Oxygenation through Manganese Oxide Burial: *Elements in Geochemical Tracers in Earth System Science*, doi:10.1017/9781108688697.
- Paiste, K. et al., 2024, Sulfur isotopes from the Paleoproterozoic Francevillian Basin record multigenerational pyrite formation, not depositional conditions: *Communications Earth & Environment*, v. 5, p. 328, doi:10.1038/s43247-024-01498-1.
- Pasquier, V., Sansjofre, P., Rabineau, M., Revillon, S., Houghton, J., and Fike, D.A., 2017, Pyrite sulfur isotopes reveal glacial–interglacial environmental changes: *Proceedings of the National Academy of Sciences*, v. 114, p. 5941–5945, doi:10.1073/pnas.1618245114.
- Pattison, D.R.M., and Forshaw, J.B., 2025, Contact-Metamorphosed to Regionally-Metamorphosed Pelites: The Natural Record: *Journal of Petrology*, v. 66, p. egaf039, doi:10.1093/petrology/egaf039.
- Pereira, M.L., Zanon, V., Fernandes, I., Pappalardo, L., and Viveiros, F., 2024, Hydrothermal alteration and physical and mechanical properties of rocks in a volcanic environment: A review: *Earth-Science Reviews*, v. 252, p. 104754, doi:10.1016/j.earscirev.2024.104754.
- Scott, G.R., Wilcox, R.E., and Mehnert, H.H., 1990, *Geology of volcanic and subvolcanic rocks of the Raton-Springer area, Colfax and Union counties, New Mexico*: U.S. Geological Survey 1507, doi:10.3133/pp1507.
- Thode, H.G., Monster, J., and Dunford, H.B., 1961, Sulphur isotope geochemistry: *Geochimica et Cosmochimica Acta*, v. 25, p. 159–174, doi:10.1016/0016-7037(61)90074-6.
- Tomkins, A.G., 2010, Windows of metamorphic sulfur liberation in the crust: Implications for gold deposit genesis: *Geochimica et Cosmochimica Acta*, v. 74, p. 3246–3259, doi:10.1016/j.gca.2010.03.003.
- Wallace, P., and Carmichael, I.S.E., 1992, Sulfur in basaltic magmas: *Geochimica et*

- Cosmochimica Acta, v. 56, p. 1863–1874, doi:10.1016/0016-7037(92)90316-B.
- Wanek, A.A., Read, C.B., Robinson, G.D., Hays, W.H., and McCallum, M.L., 1964, Geologic map of the Philmont Ranch region, New Mexico: IMAP, doi:10.3133/i425.
- Werne, J.P., Hollander, D.J., Lyons, T.W., and Sinninghe Damsté, J.S., 2004, Organic sulfur biogeochemistry: Recent advances and future research directions, *in* Sulfur Biogeochemistry - Past and Present, Geological Society of America, doi:10.1130/0-8137-2379-5.135.
- Yallup, C., Edmonds, M., and Turchyn, A.V., 2013, Sulfur degassing due to contact metamorphism during flood basalt eruptions: *Geochimica et Cosmochimica Acta*, v. 120, p. 263–279, doi:10.1016/j.gca.2013.06.025.
- Yamamoto, M., 1984, Sulfur isotope effects in the thermal breakdown of pyrite: *Earth and Planetary Science Letters*, v. 69, p. 335–340, doi:10.1016/0012-821X(84)90192-4.